SANDIA REPORT

SAND97–1562
Unlimited Release
Printed July 1998

Risk Assessment Compatible Fire Models (RACFMs)

Amalia R. Lopez, Louis A. Gritzo, Martin P. Sherman

Prepared by
Sandia National Laboratories
Albuquerque, New Mexico 87185 and Livermore, California 94550

Sandia is a multiprogram laboratory operated by Sandia Corporation, a Lockheed Martin Company, for the United States Department of Energy under Contract DE-AC04-94AL85000.

Approved for public release; further dissemination unlimited.

Sandia National Laboratories

Issued by Sandia National Laboratories, operated for the United States Department of Energy by Sandia Corporation.

NOTICE: This report was prepared as an account of work sponsored by an agency of the United States Government. Neither the United States Government, nor any agency thereof, nor any of their employees, nor any of their contractors, subcontractors, or their employees, make any warranty, express or implied, or assume any legal liability or responsibility for the accuracy, completeness, or usefulness of any information, apparatus, product, or process disclosed, or represent that its use would not infringe privately owned rights. Reference herein to any specific commercial product, process, or service by trade name, trademark, manufacturer, or otherwise, does not necessarily constitute or imply its endorsement, recommendation, or favoring by the United States Government, any agency thereof, or any of their contractors or subcontractors. The views and opinions expressed herein do not necessarily state or reflect those of the United States Government, any agency thereof, or any of their contractors.

Printed in the United States of America. This report has been reproduced directly from the best available copy.

Available to DOE and DOE contractors from
Office of Scientific and Technical Information
P.O. Box 62
Oak Ridge, TN 37831

Prices available from (615) 576-8401, FTS 626-8401

Available to the public from
National Technical Information Service
U.S. Department of Commerce
5285 Port Royal Rd
Springfield, VA 22161

NTIS price codes
Printed copy: A03
Microfiche copy: A01

SAND97-1562
Unlimited Release
Printed July 1998

Risk Assessment Compatible Fire Models (RACFMs)

Amalia R. Lopez
Aerosciences and Compressible Fluid Mechanics

Louis A. Gritzo
Unsteady and Reactive Fluid Mechanics

Martin P. Sherman
Nuclear Technology Research

Sandia National Laboratories
P. O. Box 5800
Albuquerque, NM 87185-0825

Abstract

A suite of Probabilistic Risk Assessment Compatible Fire Models (RACFMs) has been developed to represent the hazard posed by a pool fire to weapon systems transported on the B52-H aircraft. These models represent both stand-off (*i.e.* the weapon system is outside of the flame zone but exposed to the radiant heat load from fire) and fully-engulfing scenarios (*i.e.* the object is fully covered by flames). The approach taken in developing the RACFMs for both scenarios was to consolidate, reconcile, and apply data and knowledge from all available resources including: data and correlations from the literature, data from an extensive full-scale fire test program at the Naval Air Warfare Center (NAWC) at China Lake, and results from a fire field model (VULCAN). In the past, a single, effective temperature, T_f, was used to represent the fire. The heat flux to an object exposed to a fire was estimated using the relationship for black body radiation*, σT_f^4. Significant improvements have been made by employing the present approach which accounts for the presence of temperature distributions in fully-engulfing fires, and uses best available correlations to estimate heat fluxes in stand-off scenarios.

* $\sigma=5.67\text{x}10^{-8}$ W/(m^{2}K^4)

Acknowledgment

This work was sponsored by the Defense Special Weapon Agency, Department of Defense. Additional support was obtained from Sandia National Laboratories which is operated by Sandia Corporation, a Lockheed Martin Company, for the United States Department of Energy under Contract DE-AC04-94AL85000.

The authors would like to acknowledge Vernon F. Nicolette (Department 9116) for his great assistance in the numerical simulations.

Table of Contents

List of Figures

List of Tables

1.0 Introduction

1.1 Background

Numerous Weapon System Safety Assessments have identified fire as a dominant risk in the transportation and storage of nuclear weapons. The ability to predict the hazard posed by a fire still requires "the use of considerable engineering approximation."[1] Increasingly accurate and effective means must therefore be developed to improve the capability to perform fire hazard predictions, and hence the fidelity of safety assessments of weapons and other engineered systems.

A large number of scenarios must be addressed to thoroughly assess the fire survivability of an engineered system. Many of these scenarios include exposure to a pool fire which occurs, for example, as a result of a transportation accident. The prediction of fire, and its interaction with flammable and non-flammable objects, from first principles are "grand challenges". These challenges arise since fire is a highly-transient, natural balance of coupled, nonlinear phenomena with critical length and time scales spanning 5 and 7 orders-of-magnitude, respectively. Burning of a stagnant liquid fuel, *e.g.* a pool fire, is a natural balance between fuel gasification due primarily to radiative heat transfer, air entrainment and the turbulent mixing of air with fuel vapor, energy production from combustion, and the transport of energy due to advection and thermal radiation.

The goal of representing this natural balance and numerically predicting fire environments poses unique and challenging requirements for model formulation, algorithm development, and advanced computational hardware. The development of the VULCAN fire field model (*i.e.* a model which estimates the values of all relevant variables in time throughout the entire field) with such capabilities is presently underway as part of a collaborative effort established between Sandia National Laboratories (SNL) and the Norwegian Institute of Technology (NTH)/SINTEF. Efforts are also underway to develop a "next generation" fire model which will expand upon the capabilities of the existing VULCAN model. Due to the computational requirements of "first principles" numerical fire simulation, present fire modeling activities include the development of strategies to exploit best available high performance computing platforms to improve the accuracy and fidelity of large fire simulations.

Assuming the challenges of predicting the fire environment from "first principles" via fire field models can be overcome, applying such a model to each engulfing fire scenario quickly becomes intractable due to time and computer-use constraints. Probabilistic fire safety assessments have therefore historically relied on statistical methods. These techniques use existing fire data to develop temperature frequency distributions, *i.e.* distributions which statistically represent the occurrence of a different "fire temperature", T_f. The heat flux to an object for a given fire scenario is then estimated by probabilistically selecting a temperature T_f from the frequency distribution and calculating the corresponding blackbody emissive power, σT_f^4. Since data typically are restricted to a limited set of test conditions (such as wind speed, object size, shape, orientation and location, etc.), significant uncertainty is inherent when these distributions are applied to the broader range of conditions required to evaluate all potential hypothetical accident

scenarios. Furthermore, uncertainty inherent in determining the "fire temperature" is strongly amplified by the fourth order dependence which appears in the relationship used to estimate the heat flux. For example, at typical fire temperatures (1300 K), an uncertainty of +/- 100 K in T_f (~8%) results in a 62% uncertainty in the estimated heat flux to an object.

Recent efforts have therefore been focused on developing simplified deterministic fire models which reduce this uncertainty. These models incorporate a simplified deterministic formulation of the dominant variables which affect the heat flux to an object. With this approach, it is possible to reduce the uncertainty inherent in the past approaches and estimate object response trends over an expanded range of conditions since the dominant mechanisms associated with the varying fire conditions are modeled. Run times for these Risk Assessment Compatible Fire Models (RACFMs) are consistent with the requirements of a probabilistic safety (or even risk) assessment.

1.2 Objective

The objective of this work is to develop and employ models with improved predictive capabilities to represent the hazard posed by a pool fire to weapon systems transported on the B52-H aircraft. These models are developed to represent both stand-off (*i.e.* the weapons system is outside of the flame zone but exposed to the radiant heat load from the fire) and fully-engulfing scenarios (*i.e.* the object is completely covered by flames).

Achieving this objective requires the integration of all presently available resources. Two of the key resources brought to bear on this work are the VULCAN fire field model and large scale experimental data from a series of tests at the Naval Air Warfare Center (NAWC) at China Lake, CA. Brief overviews of these resources are provided below. Additional information is available from the references and authors.

1.3 VULCAN Fire Field Model

The VULCAN Advanced Fire Physics Model used in the numerical simulations is under joint development at SNL and SINTEF/NTH, and is based on the KAMELEON-II Fire Model developed at SINTEF/NTH.[2] The numerical method estimates the solution of the three-dimensional, Navier Stokes equations in finite volume form. Mathematical models used to represent various physical phenomena include the k–ε turbulence model[3], the Eddy Dissipation concept combustion model[4], and the soot model of Magnussen[5]. Thermal radiation is treated using a three-dimensional discrete transfer model.[6]

1.4 NAWC Testing Program

A considerable amount of the experimental data of interest to this work are from full-scale large-fire experiments at NAWC-China Lake. These experiments are part of several test series which comprise integrated testing and model development activities at SNL. The test program is sponsored by the Defense Nuclear Agency (DNA) and is coordinated by SNL. The objectives of this test program include supplying data required to: 1) assist in the development and calibration of RACFMs; 2) gain a better understanding of fire phenomenology; 3) assist in continuing fire field model code validation and development;

and 4) provide unique temperature and incident heat flux distributions for credible large-scale fire scenarios. Data acquired for these purposes are referenced throughout this report.

2.0 Fire Modeling Approach

The approach taken in developing the Risk Assessment Compatible Fire Models (RACFMs) for both stand-off and fully-engulfing fire scenarios was to consolidate, reconcile, and apply data and knowledge from all available resources including: data and correlations from the literature; data from a full scale test program at NAWC; and results from the VULCAN fire field model. Previous techniques for estimating the hazard posed by a fire and a description of their shortcomings is presented in the next section of this chapter. A description of the logical progression from previous models to the models presented here, including a description of the fundamental approaches employed in the newly developed models, is presented in the following sections.

2.1 Previous Approaches

Past techniques[1] have used a single, effective temperature (T_f) to represent the hazard posed by a fire. The range of fire scenarios, and the corresponding range of hazards posed by the fires which occur in these scenarios, was combined and represented by a probabilistic distribution. A "Monte Carlo" technique using this distribution was then employed to assess the hazard posed by all fire scenarios.

A probability density function (*pdf*) in the form of a three parameter Weibull distribution for the fire temperature (in ^{o}F) given by

$$pdf(T_f) = 1.77 \times 10^{-5}(T_f - 1400)^{0.83} \exp\left(-\frac{T_f - 1400}{550}\right)^{1.83} \qquad (2.1)$$

and shown in Figure 2.1 (with the temperatures converted to Kelvin) was chosen and has been used in the past. Figure 2.1 also includes the associated cumulative distribution function which describes the percentage of fires included at and below a specific fire temperature. The parameters which determine the limits of the distribution were defined based on limited fire thermocouple data appearing in the literature. No distinction is drawn between the location at which the temperature was measured, the fire scenario geometry (including fuel spill or fuel pool size and shape, and object size, geometry, location and orientation), or the environmental conditions (wind speed and directions) present during the fire. All hydrocarbon fuels are treated equally based on the general observation from the data that flame temperatures between 1030 K and 1590 K are typically observed in any hydrocarbon fuel fire. Other combustible materials were considered to burn at generally lower temperatures. Theoretical approximations of temperature within fires require consideration of the range of stiochiometry and mixing conditions present in fires. The extent to which the limits of flame temperature were defined based on theoretical analysis is evidently minimal given, for example, that the adiabatic flame temperature for JP jet fuels is approximately 500 K higher (*i.e.* 2300 K) than the upper limit of the fire temperature given by the *pdf* in Figure 2.1.

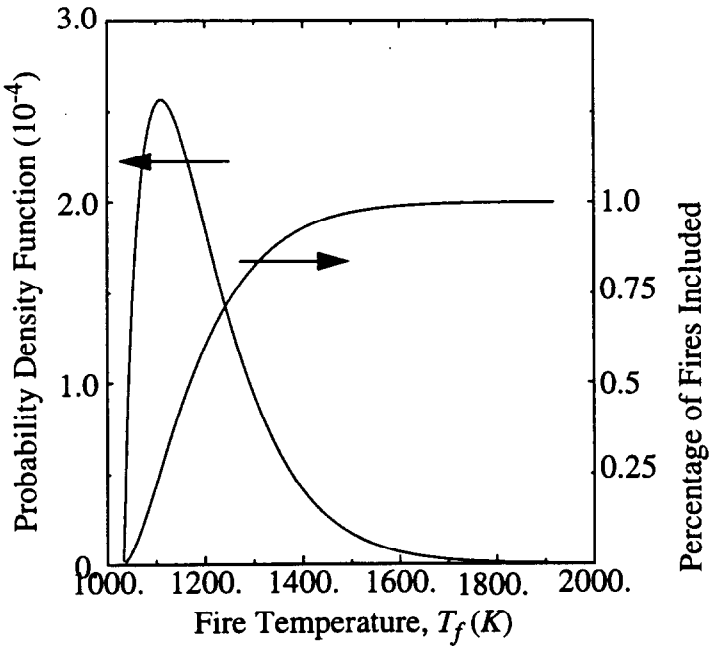

Figure 2.1 Fire Temperature Probability Density Function

A series of simplifying assumptions is invoked to calculate the heat flux from the fire temperature *pdf*. First, fires within the fully turbulent regime (*i.e.* diameter > 1.3 *m*) are assumed to be optically thick in the sense that the diameter of the fire is much larger than the optical path length. Second, for most objects of relevant size (*i.e.* dimensions ~1*m*), velocities in fires are such that convection only comprises ~10-20% of the total heat flux. Since the modeling of convective heat transfer requires a thorough knowledge of the flow field and the object geometry, it is neglected in this approach. The heat flux from the fire to an object is then estimated by the heat flux from a black body at the fire temperature, *i.e.* σT_f^4.

Significant uncertainty is associated with estimating the heat flux in this manner due to three principle phenomena. First, the nonlinear relationship between black body temperature and heat flux makes the heat flux highly sensitive to uncertainty in the fire temperature. For example, at ~ 1100 *K*, a difference of +/- 200 *K* in T_f results in factor of 2 uncertainty in the heat flux. The result of using the temperature *pdf* shown in Figure 2.1 in conjunction with the σT_f^4 relationship to calculate the heat flux is illustrated in Figure 2.2. The resulting heat flux *pdf* shown in Figure 2.2 can be regarded as the end result of previous approaches since the heat flux is the actual condition applied to the system of interest. In addition to the uncertainty associated with high sensitivity to a fire temperature which is not well-defined, existing data show a wider range of temperatures, from 800 *K* in the oxygen-starved interior* to 1700 *K* in the wake of a cylinder exposed to the wind[7], and hence a much larger range of heat fluxes, from 23 kW/m^2 to 474 kW/m^2, if the black body

* Presented later in this report.

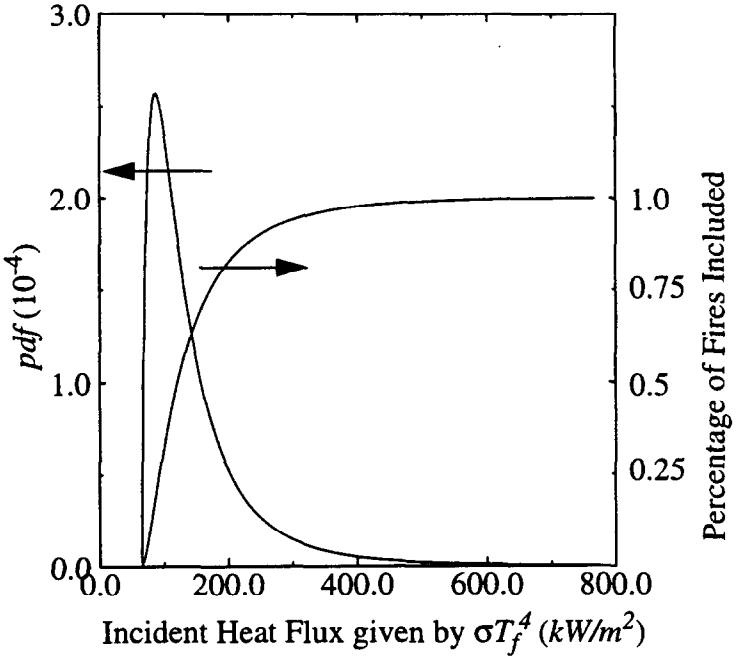

Figure 2.2 Heat Flux Probability Density Function Defined by σT_f^4

assumption is invoked. The σT_f^4 relationship also results in upper and lower limits that do not agree with data, and skews the distribution towards the low heat flux end of the range. For example, the lower limit of the heat flux shown in Figure 2.2 is 60 kW/m^2. Data[8] show heat fluxes of 20 kW/m^2 in the interior of large (18.9 m diameter) JP-8 pool fires. Figure 2.2 indicates that 29% of all scenarios involve heat fluxes between 60 kW/m^2 and 80 kW/m^2. There is no physical reasoning that supports such a distribution that is heavily-weighted towards a narrow band on the low end of the overall range. Although a thorough review of all data has not been performed, it is counter-intuitive that almost a third of the measured heat fluxes would fall within a 20 kW/m^2 window. On the upper end of the range, the distribution in Figure 2.2 shows that 92% of all scenarios result in heat fluxes less than 250 kW/m^2. This upper limit is lower than expected, as supported by data which show that large objects subjected to the medium speed (20 *MPH*) winds are consistently subjected to heat fluxes of 250-300 kW/m^2.

The second phenomenon not represented by using the preceding technique to estimate the heat transfer to an object in a fire is the *spatial distribution* of temperature and soot (and hence radiative properties). Although fully turbulent fires are optically thick overall, data and physical arguments regarding the thickness of mixing layers, and hence the flame zones, tend to show that the temperature and potentially soot (*i.e.* radiative properties) within fires are not constant within 1-3 optical paths and hence the variation must be considered to accurately calculate the incident heat flux.

The third phenomena not represented by this approach is the coupling, both radiative and convective, which occur between an object and the fire environment. Radiative coupling occurs when a comparatively cold object reduces the incident heat flux by up to 65% due to radiative cooling of the nearby flames. Analyses have been performed which allow an assessment of the influence of radiative coupling based on the value of two non-dimensional parameters.[9] Convective coupling, due to object-induced turbulence occurs when the presence of an object alters and often enhances the flow, mixing, and hence combustion, processes within the fire. These features have been observed in the wake of an object subjected to a crosswind where enhanced mixing resulted in a factor of 2 increase in the heat flux. The restriction of the air flow entrained by the fire has been shown to produce a flame attached to the surface of an otherwise non-engulfed object adjacent to the fire. This "flame holder effect" has been shown to increase the heat flux to the object by a factor of 2.5.

Significant improvements can be expected if the dominant physical phenomena which define the characteristics of large fires can be represented using deterministic models. The present work represents a logical progression from existing techniques towards dominant-physics-based models. The main improvement of this work is the ability to account for the spatial variation of temperature within the flame zone. The systems of interest in the present study, *e.g.*, the aircraft fuselage, wings, and other exterior components, are of insufficient thermal mass for radiative coupling to be important.[9] Simulation of convective coupling requires modeling of the flow field which is beyond the scope of the present approach. Future improvements in dominant-physics-based models must therefore focus on computationally tractable techniques for representing the flow and mixing processes.

As the ability to represent the fire environment by simulating the dominant physical phenomena is developed, additional importance is placed on the ability to perform credible assessment of the probability of different scenarios. In comparison to previous approaches which submitted a heat flux distribution for *all* scenarios, dominate-physics-based models reduce the uncertainty by yielding credible first order estimates of the expected heat flux for *every* scenario. Probabilistic assessment techniques are relied upon to define the likelihood of that each scenario will be encountered.

2.2 Present Stand-Off Fire Model

The stand-off fire model is based on the best available information from the literature. A detailed literature search revealed a series of correlations which represent the present state-of-the-art for estimating the heat flux from large hydrocarbon pool fires to objects outside the flame zone. After verifying the calculations and resolving some discrepancies between literature citations, the correlations were assembled into a numerical model. The validity of the approach and assumptions were then assessed by comparing model results with data from the NAWC test program. A qualitative assessment of the flame shape and flame zone exterior emissive power was performed using time-averaged photos and standard and infrared (IR) video images. The heat flux to a vertical target was assessed by comparing the model results to stand-off heat flux measurements. Discrepancies between the model and the experimental information were observed. Ongoing research is required, and is in progress, to understand and resolve these differences.

2.3 Present Fully-Engulfing Fire Model

The fully-engulfing fire model estimates the heat flux to a object subjected to a spatial temperature distribution (as opposed to a single effective flame temperature) with a 1-D participating media radiation model. The model therefore consists of two parts. First, a temperature condition submodel was developed based on NAWC data and VULCAN predictions. Scenarios with and without wind are considered. For the no-wind scenario, the available data from the NAWC test program were limited to measurements from a JP4-fueled fire. Numerical simulations of a JP4 pool fire were performed using VULCAN and were compared with the NAWC data to gain confidence in the predictive capability of the model. VULCAN was then used to expand the information set to include JP8 fuel and additional pool diameters. The temperature distribution for fires subjected to wind is obtained by rotating, scaling, and shifting the no-wind temperature profiles with the use of correlations from the literature. The temperature distribution serves as input to a 1-D radiation model that is used to calculate the heat flux on the object of interest. Radiative property trends were inferred from the available data and the participating media, *i.e.* soot, was assumed to behave as a gray absorber and emitter.

3.0 Stand-Off Fire Model

A literature review performed as part of this work revealed existing approximate methods for estimating the radiation heat transfer from large hydrocarbon pool fires to objects outside the flame zone. Examples of these methods are contained in a Society of Fire Protection Engineering (SFPE) review by Mudan and Croce[10] and in a review for the Coast Guard by Raj and Karlelkar[11]. These methods are based on the following assumptions: the exterior of the flame zone is treated as a radiating surface; the nonuniform brightness of the surface can be approximated by a suitable average obtained from experimental information; and the irregular surface can be approximated by a simple geometric shape, a finite length right circular cylinder if there is no wind, and a tilted cylinder if there is a wind. With these assumptions, the heat flux $\dot{q}$ to a small object facing the flame is

$$\dot{q} = \tau_{air} E_f F \tag{3.1}$$

where τ_{air} is the transmissivity of the air between the flame and the object, E_f is the emissive power of the flame surface, and F is the view factor from a plane element to the flame surface.

3.1 Transmissivity of the Atmosphere

The transmissivity of the air can be significantly below unity if the humidity is high and the physical path length is long. Methods of estimating the transmissivity are found in the References 10 and 11. For example, at an ambient temperature of 288 K, a path length of 50 meters, 20% relative humidity, and sea level pressure, the transmissivity is approximately 0.82. At higher elevations, the same relative humidity corresponds to a lower absolute humidity and a higher transmissivity. Since reliable relative humidity data are often not available, and to ensure conservatism, atmospheric absorption is neglected and the transmissivity is assumed to be unity. Atmospheric transmissivity can be easily added to the model if the relevant data are available.

3.2 Emissive Power of the Flame Surface

A qualitative measure of the emissive power of a flame surface can be obtained from the luminosity, *i.e.* the visible "brightness", of the surface. Large hydrocarbon pool fires are largely surrounded by an opaque smoke layer with a luminescing ring at the base of the flame zone and luminescing zones which intermittently appear higher in the plume. Mudan and Croce[10] quote several references for kerosene fires on land and gasoline fires on water which estimate that the "bright spots" occupy approximately 20% of the fire surface. Hagglund and Persson[12] suggest that the emissive power of the smoke is 20 kW/m^2 (assuming black body radiation at 800 K) and the emissive power of the bright areas is 130 kW/m^2. Using these two estimates, the average emissive power is 130(0.2) + 20(0.8) = 42 kW/m^2. One difficulty with this estimate is that it does not consider the azimuthal variation in the emissive power of the flame zone which occurs due to the effect of the wind. In general, winds create highly-luminescing standing vortices and/or fire whirls on

the leeward side of the flame zone.[13] Further studies are required to assess the impact of these well-mixed turbulent structures on the heat flux to a object located some distance from the flames. Improved models can then be developed. The present technique represents the best available information and is expected to capture the dominant physical phenomena.

3.3 Flame Height

Large hydrocarbon pool fires produce a coherent, buoyant smoke plume which continues to rise for a considerable distance as it is dispersed and diffused. Beyond the continuous flame zone, this smoke is cold and hence the emissive power of the plume exterior is negligible. To estimate the heat flux from a fire it is therefore necessary to "cut off" the radiating surface at the flame height (*i.e.*, the streamwise end of the continuous flame zone). The flame height is determined from a correlation by Thomas[14] as follows

$$\frac{H_w}{D} = 55\left(\frac{\dot{m}}{\rho_a\sqrt{gD}}\right)^{0.67}\tilde{u}^{(-0.21)} \quad , \tag{3.2}$$

where H_w is the flame height with wind, D is the pool diameter, $\dot{m}$ is the fuel mass burning rate, ρ_a is the air density, g is the gravitational acceleration (9.8 m/s^2), and $\tilde{u}$ is the nondimensional wind velocity defined as

$$\tilde{u} = \frac{u}{(gD\dot{m}/\rho_v)^{\frac{1}{3}}} \quad , \tag{3.3}$$

where ρ_v is the density of the unburned fuel vapor. A fuel recession rate of 0.06 mm/s (based on NAWC experimental data for JP8-fueled fires) is used to determine the fuel mass burning rate.

The correlation for flame height given in Equation 3.2 does not apply in the limit as the wind velocity goes to zero. For the zero wind speed case, Thomas' revised correlation for the flame height is given by

$$\frac{H}{D} = 42\left(\frac{\dot{m}}{\rho_a\sqrt{gD}}\right)^{0.61} \quad . \tag{3.4}$$

For very low wind speeds, if H_w is larger than H, H is used as the flame height.

3.4 Flame Zone Tilt and Wind Drag

The flame zone shape is approximated by a vertical circular cylinder without wind, and by a tilted cylinder with wind as shown in Figure 3.1. Various correlations exist for estimating the angle of tilt from the vertical. The present stand-off fire model uses the correlation by the American Gas Association[15] as follows:

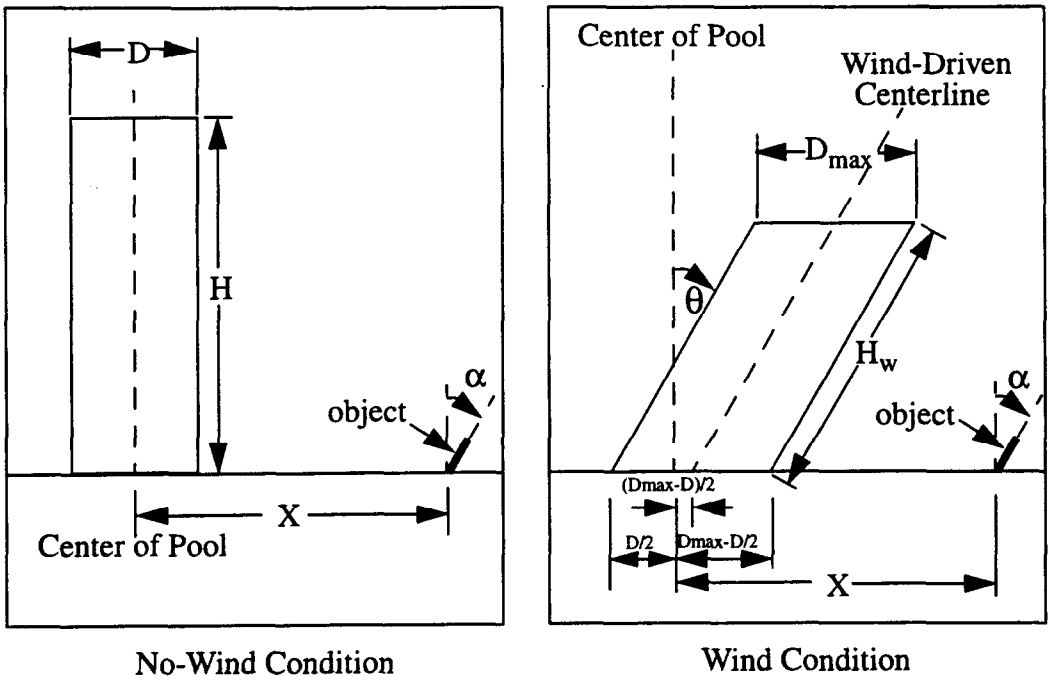

Figure 3.1: Flame Zone Shape for No-Wind Condition and Wind Condition

$$\cos\theta = 1/(\sqrt{\bar{u}}) \tag{3.5}$$

for a nondimensional wind speed above unity. If the nondimensional wind speed is unity or less, the angle of tilt is assumed to be zero.

In addition to tilting the flame zone, wind causes the leeward side of the flame zone to extend beyond the pool diameter along the direction of the wind. This phenomena is referred to as "wind drag". The diameter of the flame zone normal to the wind direction remains unchanged. The shape near the ground is therefore given by an ellipse where the center of the ellipse is shifted downwind from the center of the fuel pool. If the minor diameter of the ellipse is D (the pool diameter) and the major diameter of the ellipse is D_{max}, the center of the ellipse is shifted downwind by $(D_{max}-D)/2$ from the pool center as shown in Figure 3.1. The major diameter is determined from the correlation found in Reference 10 as follows:

$$\frac{D_{max}}{D} = 1.25(Fr)^{0.069}(\rho_a/\rho_v)^{0.48} \tag{3.6}$$

where Fr is the Froude number and is equal to $u^2/2g$. For low wind speeds, if the above correlation results in a value of D_{max} less than D, D_{max} is set equal to D.

3.5 Radiation View Factors

Once the flame zone shape is determined given the wind conditions, the radiation view factor (F) from a plane element, *i.e.* a target, to a tilted cylinder can be determined from analytical expressions by Mudan.[10,16] Results are given for vertical (F_v) and horizontal (F_h) targets in the plane of tilt (downwind and upwind directions) and in the plane normal to the plane of tilt (crosswind). The view factor to the target is given by

$$F = F_v \cos\alpha + F_h \sin\alpha \,, \tag{3.7}$$

where α is the angle of tilt of the element from the vertical. The view factor for maximum flux, F_{max}, is simply $F_{max} = \sqrt{F_v^2 + F_h^2}$ which occurs when the angle from the vertical is given by $\alpha_{max} = \text{atan}(F_v/F_h)$. The expressions for the view factors F_v and F_h are tedious and are therefore given in Appendix A. While developing the model, several typographical errors where discovered in the existing literature. Corrected expressions are given here. Additional information, including plots of the maximum flux results in the upwind, downwind and cross wind directions, and the angle from the vertical for maximum flux to an element, are presented in internal memos by Sherman.[17,18]

4.0 Fully-Engulfing Fire Model

The fully-engulfing fire model provides the heat flux to a surface of an engulfed object by estimating the temperature distribution in the neighborhood of the surface and calculating the heat flux using a 1-D participating media radiation model. Temperature distribution estimates are obtained along a vector normal to the surface using correlations based on experimental data and VULCAN model predictions. The effect of the wind on the temperature distribution is treated by shifting, rotating, and scaling the no-wind temperature distribution using correlations in the literature. To account for the influence of the heated ground surface on the heat flux to the object, it was also necessary to determine the temperature at a point on the ground outside of the fire. A ground temperature model was therefore developed. Radiative property trends comprised of a range of absorption coefficients were identified through the use of data from full scale tests performed at NAWC.

4.1 Temperature Condition Submodel

Simulations using the VULCAN fire field model were performed to develop a temperature condition submodel. Due to the availability of existing data, VULCAN simulations of a 18.9 *m* diameter JP4 pool fire under no-wind conditions were performed first. Centerline temperatures and radial temperature profiles were compared with experimental data from tests at NAWC. It was determined that the model predictions were very sensitive to grid density and domain size. An optimum grid density and domain size, *i.e.* a final grid, was determined for which the predictions agreed very well with the data. As expected, the numerical predictions also compared favorably to the correlations by Sherman which represent the same data.[19] With this measure of confidence that the VULCAN model can predict the trends evident in the experimental data, simulations of other conditions (including those beyond the range of existing data) were performed to assist in the development of an appropriate submodel. With the final grid determined from the JP4 simulations, JP8 simulations were performed for the no-wind case and correlations were developed from the numerical data. Due to the lack of no-wind data for a JP8 pool fire, the numerical predictions were compared with low wind experimental data from a NAWC JP8 test and good agreement was still obtained.

Temperature data from tests at NAWC were taken using thermocouples. These data therefore represent the temperature at the thermocouple junction. The temperatures predicted by the model represent estimates of the local temperature of the absorbing and emitting media. There are many heat transfer mechanisms which can cause significant differences between these two temperatures.[20] Given the purpose of the RACFMs (*i.e.* to obtain first order estimates of the heat flux to an object within the run time restraints of probabilistic safety assessments), these differences are only qualitatively considered when comparing the temperature distribution magnitudes and trends. Although not considered here, the fundamental differences between thermocouple and local media temperature must be addressed during model validation. Consistency is, however, maintained throughout the radiation calculation performed by the RACFMs since both the temperature and radiative property distributions are based on thermocouple measurements.

4.1.1 JP4 VULCAN Simulations

Due to the availability of existing data from the NAWC test program, a VULCAN simulation of a JP4 pool fire under no-wind conditions was performed to gain confidence in the trends predicted by the code. The use of several different grids was explored. The final domain size used in the simulation of a 18.9 *m* diameter pool fire ranged from -100.0 to 100.0 *m* in the *x* direction, from 0.0 to 100.0 *m* in the *y* direction, and from 0.0 to 60.0 *m* in the *z* direction. The fuel pool was located at z=0.0 *m* and the region surrounding the fuel pool at z=0.0 was represented as a flat, solid boundary. At the z=60.0 *m* boundary, a constant pressure condition was specified. Constant pressure conditions were also specified at the x=-100.0 *m* boundary, the x=100.0 *m* boundary, and the y=100.0 *m* boundary. At the y=0.0 *m* boundary, a symmetry condition was specified to allow simulation of only half of the problem. Table 4.1 lists the fuel properties used in the numerical simulation of the JP4 and the JP8 pool fires. A specified fuel evaporation rate was used in the simulations. Although VULCAN will estimate the fuel evaporation rate based on the radiative heat flux to the fuel surface, the rate calculated by VULCAN was almost a factor of two larger than the rate observed during the experiments. Revision of the fuel gasification model in VULCAN is presently underway.

Table 4.2 describes the grids which were used in the simulations. Initially, a symmetric grid (not listed in Table 4.2) was created with the first grid point very close to the pool (z=0.2 *m*) in order to extract the numerical results at the same elevations as the thermocouple measurements in the NAWC tests. This grid produced a fire that was tilted in the *x*-direction even though the domain and boundary conditions were symmetric about the pool center. It appeared that the problem was related to placing the first grid point too close to the pool in combination with attempting to simulate the less stable no-wind case. For a no-wind simulation, constant pressure boundaries are specified around the domain and the model calculates the velocities. In a wind simulation, constant velocities are specified around the domain. This condition is mathematically easier to solve since constant pressure boundaries can yield either inflow or outflow. Many different simulations were performed to try and eliminate this anomaly in the solution. The fire did not tilt if the first grid point above the pool was moved from 0.2 *m* to 0.5 *m* (Grid #1) or if the outer boundaries in both the *x* and *y* directions were moved from 80 *m* to 100 *m* for the 0.2 *m* grid (Grid #2). To better resolve the high gradients near the pool, it is necessary to keep the first grid point above the pool at 0.2 *m*. To prevent the fire from tilting, constant pressure boundaries should be located sufficiently far, *e.g.* 100 *m*, from the flame zone to ensure that buoyancy-induced velocities have a negligible affect on the pressure field at the boundaries.

Figure 4.1 shows the centerline temperature predictions for both grids (Grid #1 and Grid #2) compared to the NAWC experimental data for a JP4 pool fire. The Grid #2 results are in much better agreement with the data than the Grid #1 results. This trend was expected because the high gradients near the pool are better resolved when the grid points are moved closer to the pool. In an attempt to ensure grid convergence, another simulation was performed with a grid (Grid #3) which had the first grid point located at 0.1 *m* above the pool. Contrary to expectations, this grid produced results that were between the Grid #1 results and the Grid #2 results. Closer examination of the Grid #3 solution indicated that

large asymmetries had developed at the base of the fire which were affecting the results. Also note that the Grid #2 produced less severe asymmetries at the base of the fire and Grid #1 produced a symmetric fire. This series of observations leads us to believe that the asymmetries were linked to the aspect ratio of the cells. In all the above cases, the spacings in the other two directions were held fixed as the first set of grid points were moved closer to the pool.

The next series of simulations were performed in an attempt to eliminate the asymmetries at the base of the fire. All the previous grids had the grid points spaced approximately 1.0 *m* apart in both the *x* and *y* directions across the pool. Therefore, the cell aspect ratio increased with decreasing distance between the first grid point and the pool surface. For Grid #2, the aspect ratio (vertical/horizontal) of the cells next to the pool was 5. The aspect ratio was reduced to a value of 2.5 by changing the grid point spacing across the pool from 1.0 *m* to 0.5 *m*. This new grid (Grid #4) did remove the asymmetries at the base of the fire but it also produced a fire with continuous puffing. In past simulations, a steady fire shape was obtained due to the numerical viscosity associated with the first-order upwind differencing scheme which tends to damp out the large-scale vortical structures. However, as the number of grid points is increased, the numerical viscosity associated with the first-order upwind scheme is reduced. This reduction causes the fire to continue puffing beyond the initial puff associated with ignition. Figures 4.2-4.7 show the *time-averaged* temperatures obtained using Grid #4. Significant deviations were observed between the experimental data and the results obtained using Grid #4.These differences may be due to incompatibilities of the submodels in VULCAN under unsteady conditions. For example, the applicability of the k-ε turbulence model in conjunction with large scale unsteady "puffing" is an issue of present research which is beyond the scope of this study. Since the intent of this work is to only look at steady state fires, additional grids were investigated.

Finally, a grid (Grid #5) with an aspect ratio of 3.75 (between 2.5 and 5.0) was generated in hopes of eliminating the asymmetries at the base of the fire volume while not producing a fire with continuous puffing. Grid #5 did not appear to produce a puffing fire. There were, however, small differences in the temperature values with time. Some slight changes in the shape of the fire volume with time are consistent with the formulation of the model and so time averaged temperatures were used for comparison with the data. In addition, Grid #5 did produce small asymmetries at the base of the fire volume but they were not as severe as the Grid #2 results. Figure 4.2 also shows the centerline temperatures obtained using the Grid #5 as compared to the Grid #2 solution, the Grid #4 solution, the experimental data, and the Sherman correlation values. Again, Grid #5 centerline temperature results were consistently less than the data. However, the thermocouple temperature measurements are expected to be higher than the gas temperature along the centerline because the thermocouple is absorbing heat from the peak temperature region which surrounds the centerline. Also as expected, these results fall between the other two numerical results. Figures 4.3-4.7 show Grid #5 radial temperature profiles at five elevations as compared with the other numerical predictions, the experimental data, and the Sherman correlation values. At every elevation, Grid #5 temperature profiles agree well with the experimental data. The peak temperature location occurs further away from the centerline than the Grid #4 predictions and the results are in general closer to the Grid #2 solution. Note that the differences between the numerical predictions and the experimental

data outside of the predicted region of the flame zone are due to the radiation between the thermocouple and the fire. Overall, the numerical results produced with Grid #5 show the best agreement with the experimental data. Reducing the aspect ratio further will cause the fire to puff continuously and while, this is physically real, it was the intent of this study to only look at steady state fires.

4.1.2 JP8 VULCAN Simulations

VULCAN was used to simulate a JP8 pool fire under no-wind conditions to provide data for a correlation. The same grid used in the JP4 simulation (Grid #5) was also used in a quiescent JP8 18.9 *m* diameter pool fire simulation. Unfortunately, experimental data are only available for a low wind case. Figure 4.8 shows the wind direction relative to the array of thermocouple poles used in the NAWC test. The wind was approximately 1.34 *m/s* and the wind direction is 37.5 degrees from the array. Despite these differences, these data can provide a first order comparison of the radial profile shapes generated by the model. Figure 4.9 shows a comparison of the time averaged temperatures along the centerline for JP8 and JP4 simulations. As expected, the JP4 values are slightly lower than the JP8 values. This trend is due to larger fuel concentrations in the vapor dome above the JP4 pool which tends to limit the combustion process in this region and produce lower temperatures.[17] In addition, two other JP8 pool fire simulations were performed with smaller (10 *m*) and larger (30.0 *m*) pool diameters. Different diameter fires were simulated to determine if the temperature curves collapse when normalized by pool radius. Figures 4.10-4.14 show the predicted temperature profiles at five elevations compared with the NAWC experimental data for a JP8 pool fire. Overall, the numerical predictions show good agreement with the experimental data. Small differences were expected because the wind was not aligned with the centerline. In addition, the temperature curves do collapse reasonably well when normalized by the pool radius with the exception of Figure 4.10 at z/Ro=0.032. Sharp gradients are likely near the surface of the pool as the fuel vapor rapidly transitions from the boiling temperature of the fuel to temperatures consistent with exposure to turbulent flame fronts. Numerical complications therefore exist near the surface of the pool. Furthermore, since fuel vaporization rates typically do not vary strongly with pool diameter, a difference in normalized results at locations very close to the fuel surface can be expected for different pool sizes. The results for the 30.0 *m* pool were unfortunately not available at z=0.3 *m* due to the grid spacing. Results on either side (z=0.15 *m* and z=0.45 *m*) are therefore shown. Based on the results presented here, and considering the spirit of the RACFMs, the temperature within the fire can be represented by a single correlation for variety of pool diameters.

4.1.3 Temperature Correlations

To illustrate the appropriate functional form, a temperature correlation was developed to represent the experimental data from a JP4 fire under quiescent conditions by Sherman.[19] Next, a temperature correlation was developed from the JP8 numerical data for a no-wind case. It was necessary to use the numerical data for the correlation because experimental data from a JP8 fire calm conditions is not presently available. The numerical

data ranged from an elevation of 0.3 m to 2.3 m above the pool surface. The form of the JP8 temperature correlation is as follows:

$$T(Z) = \frac{A(Z)}{(1 + B(Z)R^2 + C(Z)R^3 + D(Z)R^4 + E(Z)R^5)} , \quad (4.1)$$

for

$$R = r/r_o, \text{ and } Z = z/r_o$$

where r is radius from the pool center, z is the height above the pool, and r_o is the pool radius. When R is equal to zero, the centerline temperature is equal to $A(Z)$. The coefficients A, B, C, D, and E are functions of Z as follows:

$$A(Z) = a(1) + a(2)(1 - e^{-a(3)Z}) + a(4)(1 - e^{-a(5)Z}))$$

$$B(Z) = b(1) + b(2)Z + b(3)\ln(Z)^2 + b(4)\ln(Z) + b(5)e^{-Z}$$

$$C(Z) = c(1) + c(2)Z\ln(Z) + c(3)\ln(Z) + c(4)/Z^{0.05}$$

$$D(Z) = d(1) + d(2)Z + d(3)Z\ln(Z) + d4/Z$$

$$E(Z) = e(1) + e(2)Z^2 + e(3)/Z + e(4)e^{-Z} . \quad (4.2)$$

Table 4.3 lists the coefficient values for a, b, c, d, and e. The form of the temperature correlation was obtained by curve fitting the data with automated curve fitting software.[22] Overall, as shown in Figures 4.10-4.14, the correlation represents the numerical data very well.

4.2 Ground Temperature Model

A simplified ground temperature model was developed to determine the temperature at a point on the ground outside of the fire. This is necessary in cases where the ground forms the boundary of the 1-D temperature distribution. To obtain a conservative estimate of ground temperature, the ground surface is assumed to be black with no conduction into the ground and no heating of ground moisture. Similar to the Stand-Off Fire Model described in Chapter 3, the flame zone surface is assumed to be a black body radiating at 42 kW/m^2. Outside of the fire, the surroundings are assumed to be a black body at 300 K. With these assumptions, the problem can be modeled as steady-state radiant heat transfer between three black surfaces: the fire flame zone, an element on the ground, and the surroundings. The energy equation for an element on the ground then simplifies to that for a steady-state radiation energy balance as follows:

$$\sigma T_\infty^4(1 - F_h) + F_h E = \sigma T_g^4 \quad (4.3)$$

where σ is the Stefan-Boltzmann constant (5.67×10^{-8} $W/(m^2K^4)$), T_∞ is the ambient temperature (300 K), F_h is the view factor from a horizontal ground element to the fire, E is the fire black body radiative flux (42 kW/m^2), and T_g is the ground temperature which can be computed with the above equation.

As discussed in Chapter 3, the flame zone is assumed to be a vertical circular cylinder in a no-wind condition. When winds are present, the flame zone is represented by a tilted cylinder. Mudan[16] gives analytical expressions for both the height of the fire and the view factor from a horizontal element to the fire. Figure 4.15 shows the variation of the ground temperature with distance from the pool center. This example is for a 20.0 m diameter pool fire under no-wind conditions. These results show that radiant heating from the ground to an object can be important and must be considered. Additional information on the simplified ground temperature model is provided in the internal memo by Sherman.[23]

4.3 1-D Radiation Model

Due to the low velocities (< 10 m/s), high soot volume fraction, and high temperatures typical of large hydrocarbon fuel fires, the heat flux to an engulfed object is due primarily to thermal radiation. This observation is supported by the experimental study of Nakos and Keltner[24] which show convective heat fluxes to objects in large JP4 fires to be a factor of 5 to 10 less than those due to radiative heat transfer. Accordingly, RACFMs apply participating media radiative transport as the sole mode of heat transfer between the temperature distribution in the fire and the surface of the engulfed object. Furthermore, to limit computational requirements, and since the temperature gradients in the streamwise direction are typically small relative to those normal to the surface of an engulfed object, the radiative flux to the object, q_r, is determined from the temperature field by the 1-D solution of Siegel and Howell.[25] Although similar in concept, note that this technique differs from the traditional Schuster-Schwarzchild[26] or Milne-Eddington[27] two-flux approximations developed to treat atmospheric radiative transport. The method employed here uses the exact formulation of the radiative transport equation along a line of sight and invokes the exponential kernel approximation to evaluate the resulting exponential integrals. Two-flux approximations assume that the intensity is uniform over a hemisphere normal to a line of sight at all positions along the line of sight. Since the temperature (and not intensity) are assumed constant in this work, the 1-D solution using the exponential kernel approximation is preferred.

Using this technique, the flux, q_r, at the optical path length τ from the plate surface can expressed as:

$$q_r(\tau)/\sigma = T_f exp\left(-\frac{3}{2}(\tau_f - \tau)\right) - T_w^4 exp\left(-\frac{3}{2}\tau\right)$$

$$+\frac{3}{2}\int_0^{\tau_f} T^4(\tau')exp\left(-\frac{3}{2}(\tau' - \tau)\right) d\tau'$$

$$-\frac{3}{2}\int_0^{\tau_f} T^4(\tau')exp\left(-\frac{3}{2}(\tau - \tau')\right) d\tau' \quad , \tag{4.4}$$

where T_f is the temperature of the far field boundary, T_w is the temperature at the object surface, *i.e.* the wall, and τ_f is the optical path length to the farfield boundary.

Large hydrocarbon pool fires are dominated by absorption and, typically, according to the works of Longenbaugh and Matthews[28], and Felske and Tien[29], scattering can be neglected. Assuming scattering is negligible, the optical path length is defined by

$$\tau = \int_0^y \sigma_a dy' , \tag{4.5}$$

where σ_a is the absorption coefficient of the media and y is the distance along the line of sight.

Calculations of the radiative flux were performed along a line of sight normal to the surface of the object. To eliminate the influence of the location of the farfield boundary, the extent of the domain was defined by a minimum of 5 optical path lengths, *i.e.* $\tau_f = 5.0$. In the event that the boundary of the flame zone or the ground was closer than 5 path lengths from the surface of interest, a black boundary at ambient temperature or the temperature given by the ground temperature model was used respectively.

4.4 Radiative Properties

In addition to determining the temperature distribution within the fire environment (which is of primary importance since local emission depends on the temperature to the fourth power), estimating the absorption coefficient represents one of the principle challenges in the development of RACFMs.

Although efforts are presently underway to use absorption-emission spectroscopy to obtain point measurements of soot volume fraction and soot emission temperature, precise temperature distribution and absorption coefficient data for large fires are presently not available. Using *time-averaged* thermocouple temperature distributions measured normal to the fuel surface and hemispherical heat flux measurements taken at the fuel surface, a

1-D inverse radiative transfer analysis was performed to gain an improved understanding of the spatial variation of the extinction coefficient. Estimates of the media temperature distribution are provided by thermocouple temperature measurements. Use of these estimates, in conjunction with measured heat fluxes to determine radiative properties is subject to the discrepancies inherent between thermocouple and actual media temperatures[20] and the assumption that the temperature distribution is uniform within the hemisphere above the fuel surface. Although this technique yields "effective" (as opposed to true) absorption coefficients, it does represent a consistent approach throughout this effort since thermocouple temperatures and 1-D radiative transfer techniques are used in the RACFMs.

Temperature distribution, heat flux to the fuel surface, and effective absorption coefficient data are shown in Figure 4.16 for a 18.9 *m* JP8 pool fire under low wind conditions. The data show that the effective absorption coefficient varies between 1 m^{-1} and slightly greater than 5 m^{-1} and tends to decrease with distance from the center of the pool. This range of absorption coefficient is consistent with other results from JP4 fires.[20]

Accordingly, values of the absorption coefficient of both 1 m^{-1} and 5 m^{-1} are used in the RACFMs. The largest resulting heat flux to the surface is provided as the most conservative estimate.

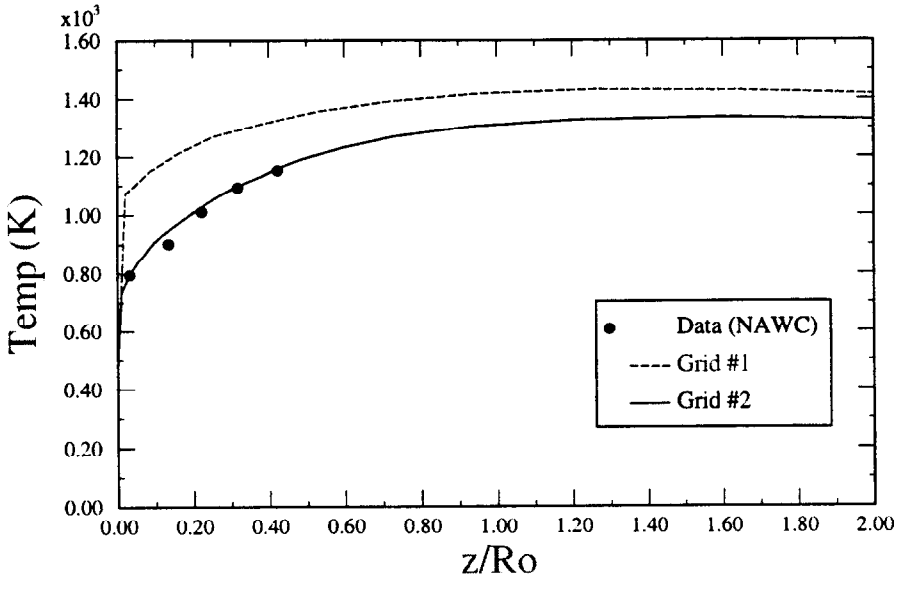

Figure 4.1: Centerline Temperature Variation of Numerical Predictions and Experimental Data for a JP4 Pool Fire

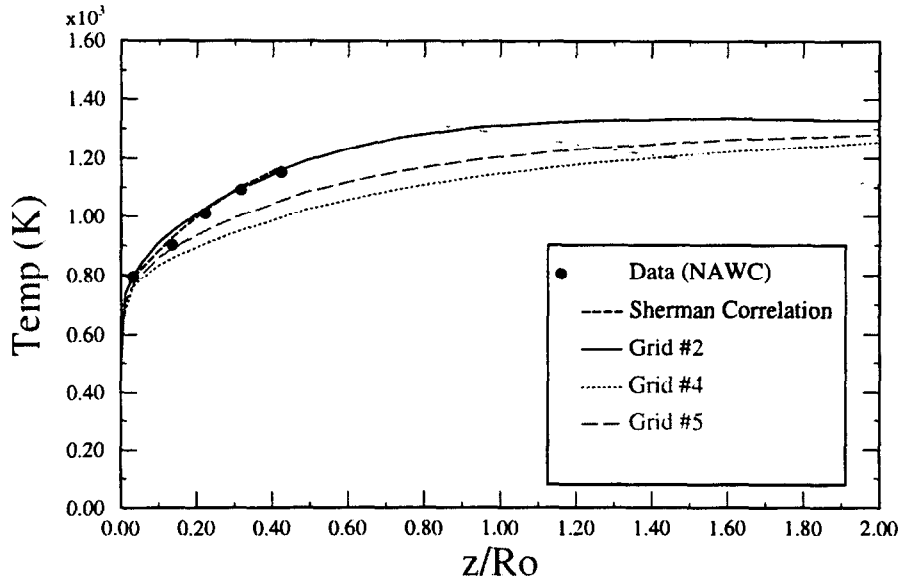

Figure 4.2: Centerline Temperature Variation of Numerical Predictions, Sherman Correlation, and Experimental Data for a JP4 Pool Fire

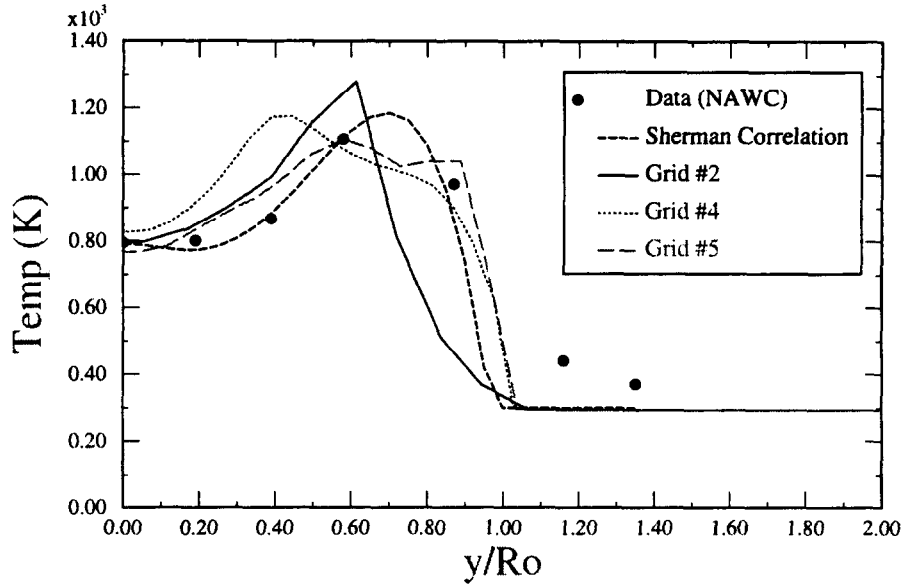

Figure 4.3: Radial Temperature Variation at *z/Ro*=0.032 of Numerical Predictions, Sherman Correlation, and Experimental Data for a JP4 Pool Fire

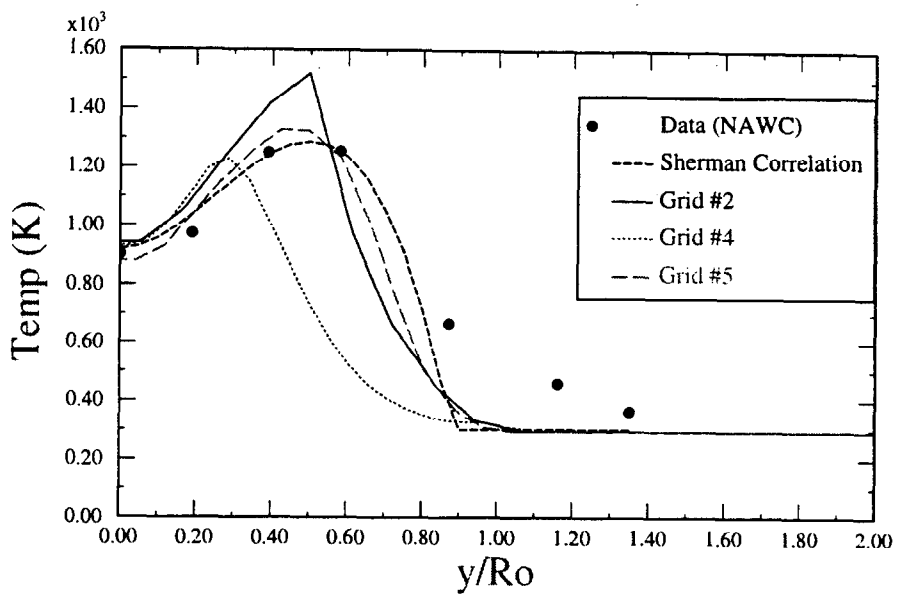

Figure 4.4: Radial Temperature Variation at *z/Ro*=0.127 of Numerical Predictions, Sherman Correlation, and Experimental Data for a JP4 Pool Fire

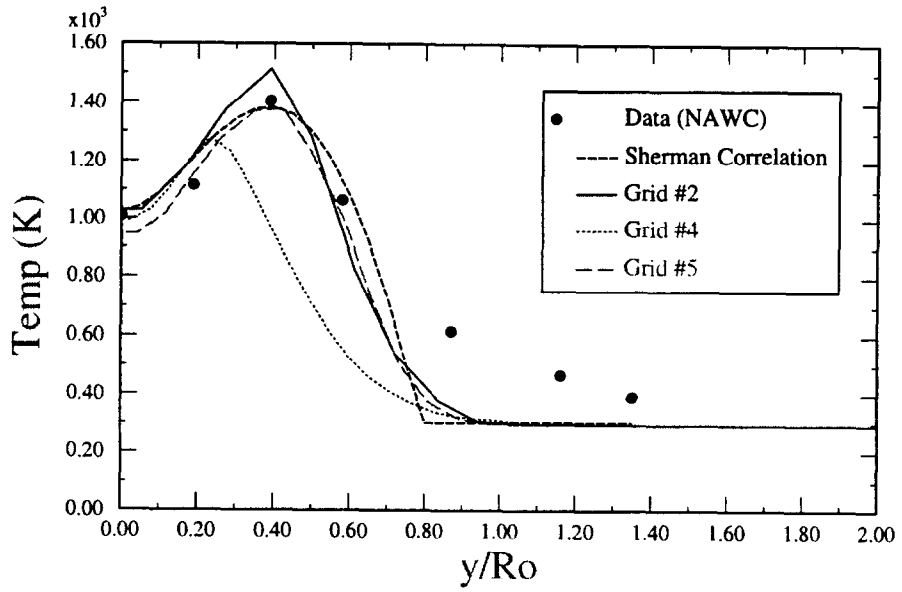

Figure 4.5: Radial Temperature Variation at *z/Ro*=0.222 of Numerical Predictions, Sherman Correlation, and Experimental Data for a JP4 Pool Fire

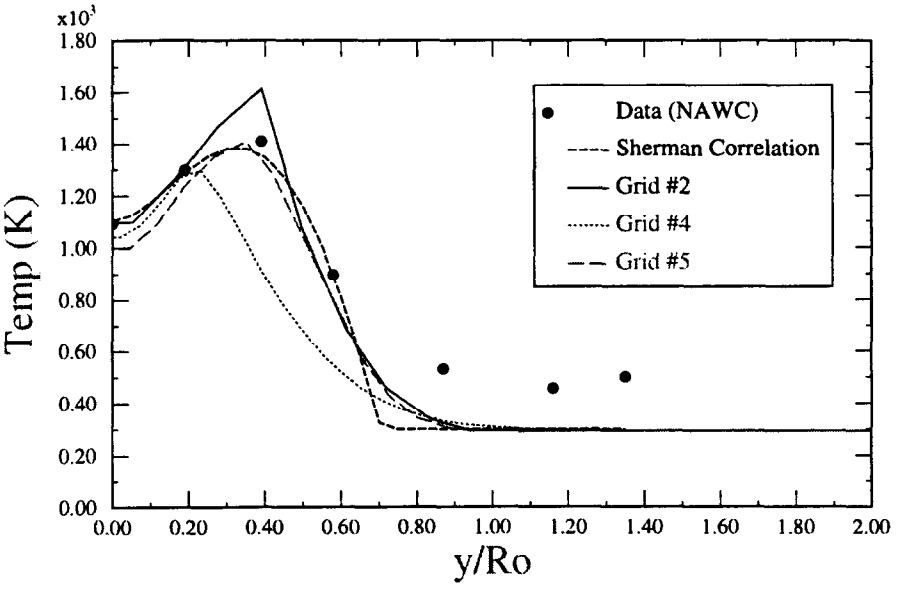

Figure 4.6: Radial Temperature Variation at *z/Ro*=0.317 of Numerical Predictions, Sherman Correlation, and Experimental Data for a JP4 Pool Fire

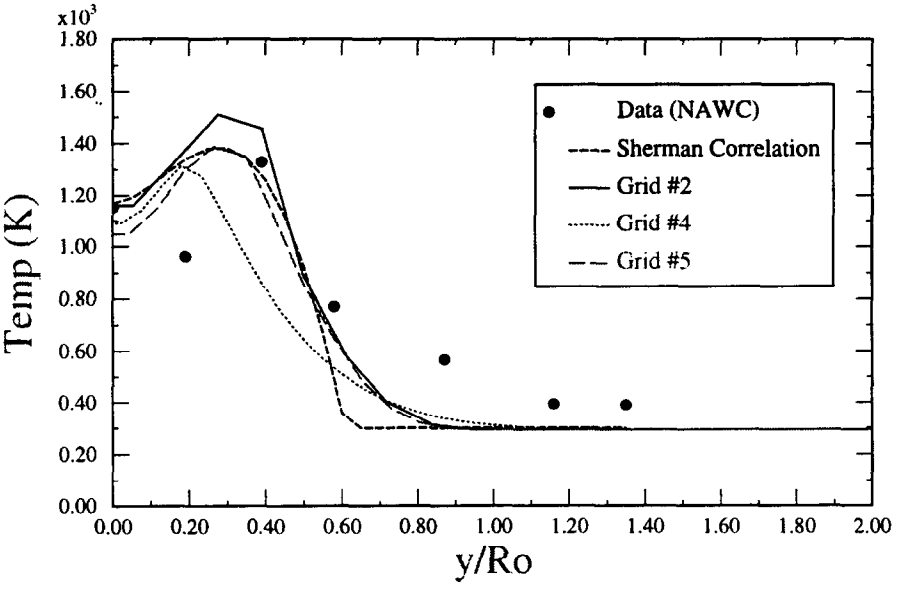

Figure 4.7: Radial Temperature Variation at *z/Ro*=0.423 of Numerical Predictions, Sherman Correlation, and Experimental Data for a JP4 Pool Fire

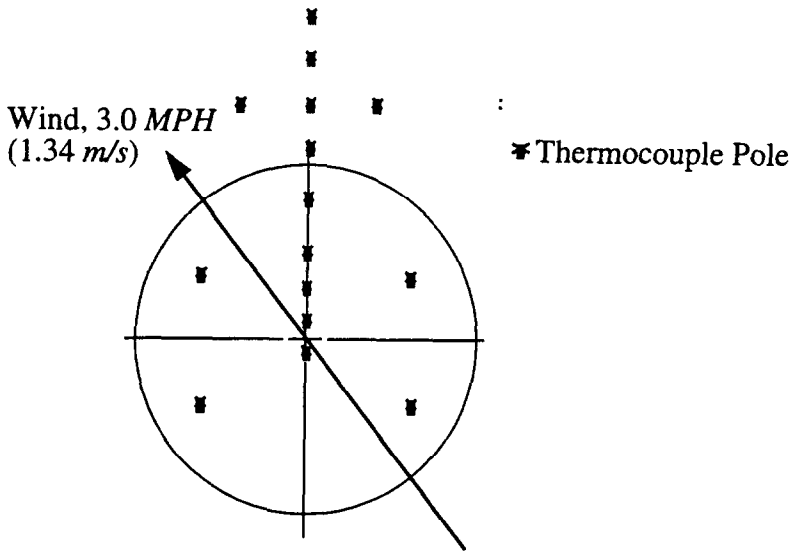

Figure 4.8: Low Wind NAWC Test of JP8 Pool Fire

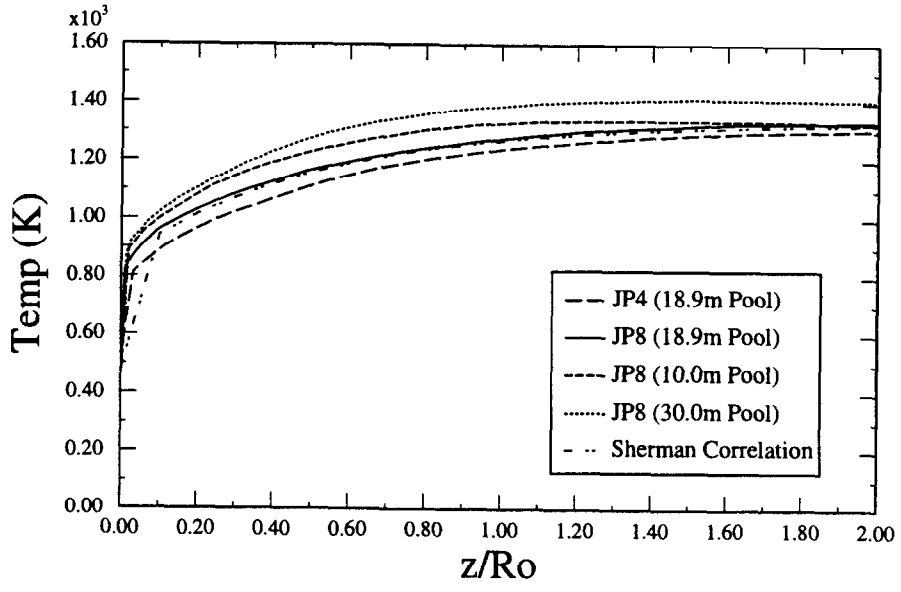

Figure 4.9: Centerline Temperature Variation of JP4 Numerical Prediction, JP8 Numerical Predictions, Sherman Correlation, and Experimental Data for a JP8 Pool Fire

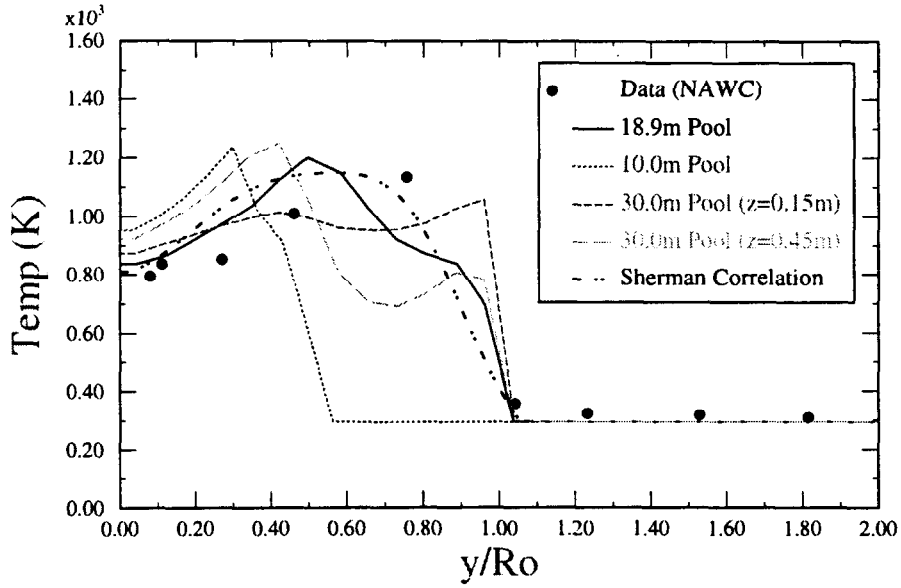

Figure 4.10: Radial Temperature Variation at *z/Ro*=0.032 of Numerical Prediction, Sherman Correlation, and Experimental Data for a JP8 Pool Fire

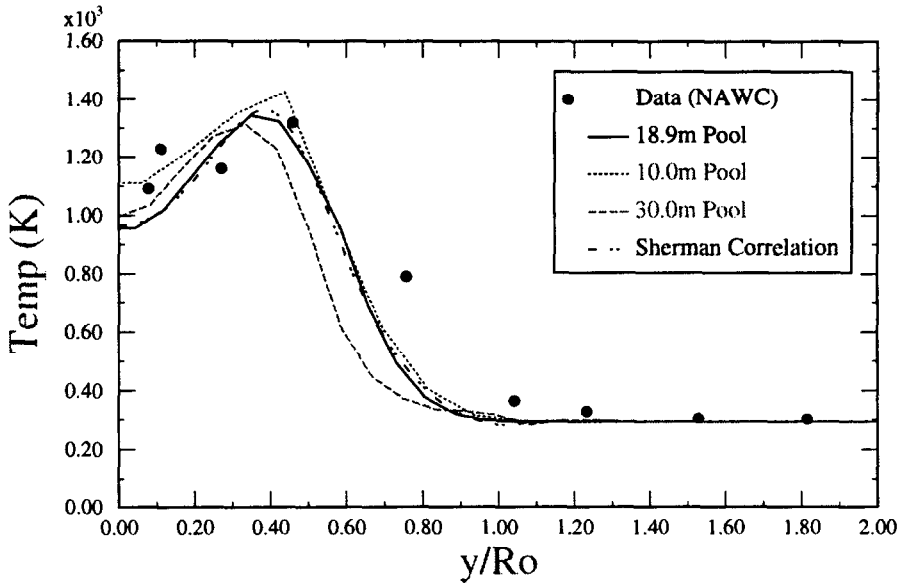

Figure 4.11: Radial Temperature Variation at z/Ro=0.127 of Numerical Predictions, Sherman Correlation, and Experimental Data for a JP8 Pool Fire

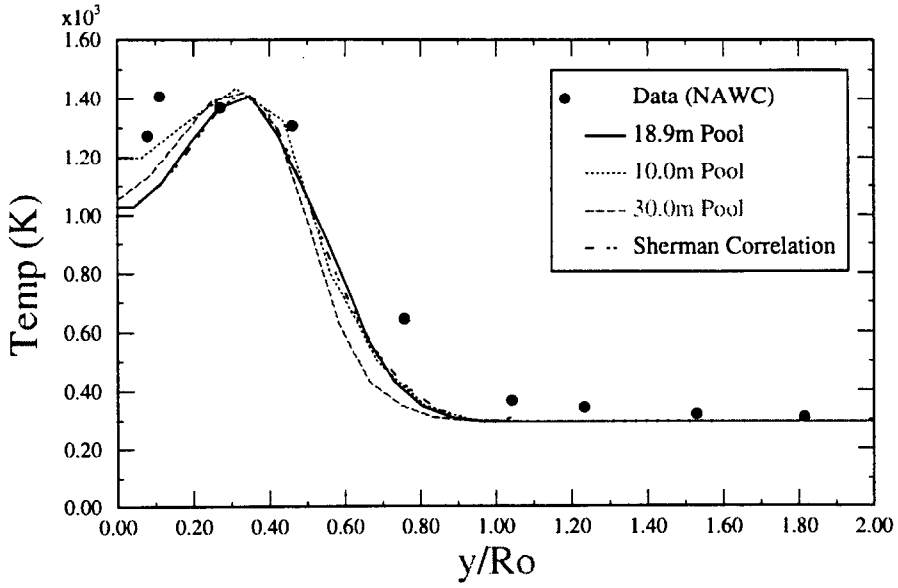

Figure 4.12: Radial Temperature Variation at z/Ro=0.222 of Numerical Predictions, Sherman Correlation, and Experimental Data for a JP8 Pool Fire

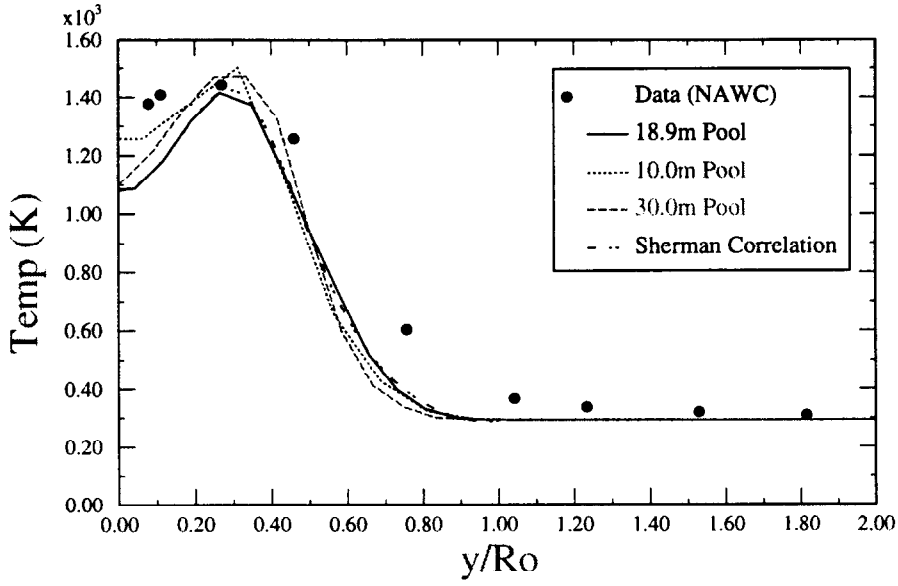

Figure 4.13: Radial Temperature Variation at *z/Ro*=0.317 of Numerical Predictions, Sherman Correlation, and Experimental Data for a JP8 Pool Fire

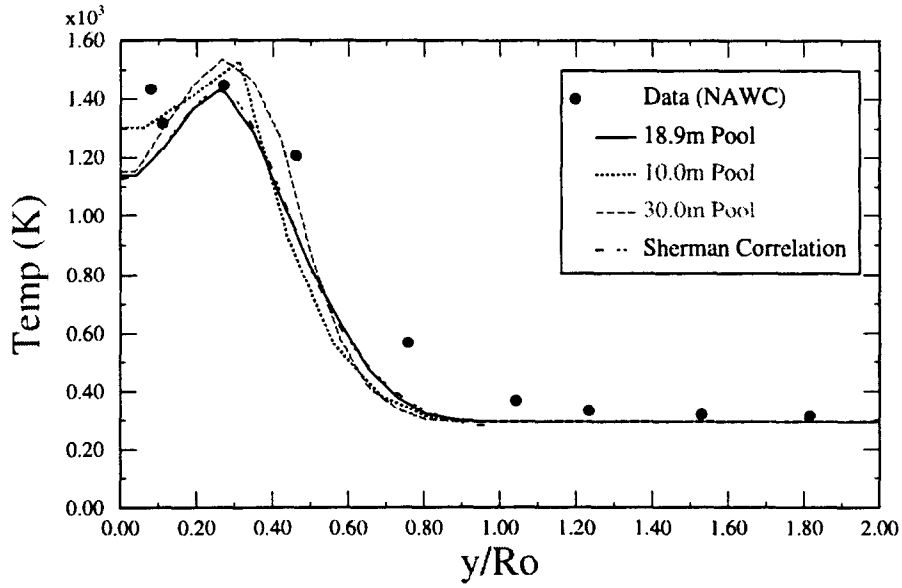

Figure 4.14: Radial Temperature Variation at z/Ro=0.423 of Numerical Predictions, Sherman Correlation, and Experimental Data for a JP8 Pool Fire

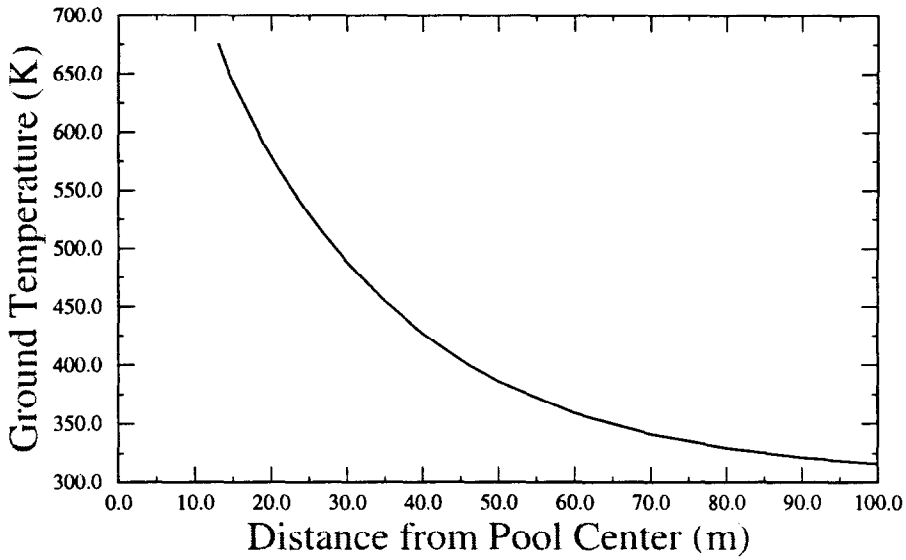

Figure 4.15: Ground Temperature From Pool Fire Under No-Wind Conditions

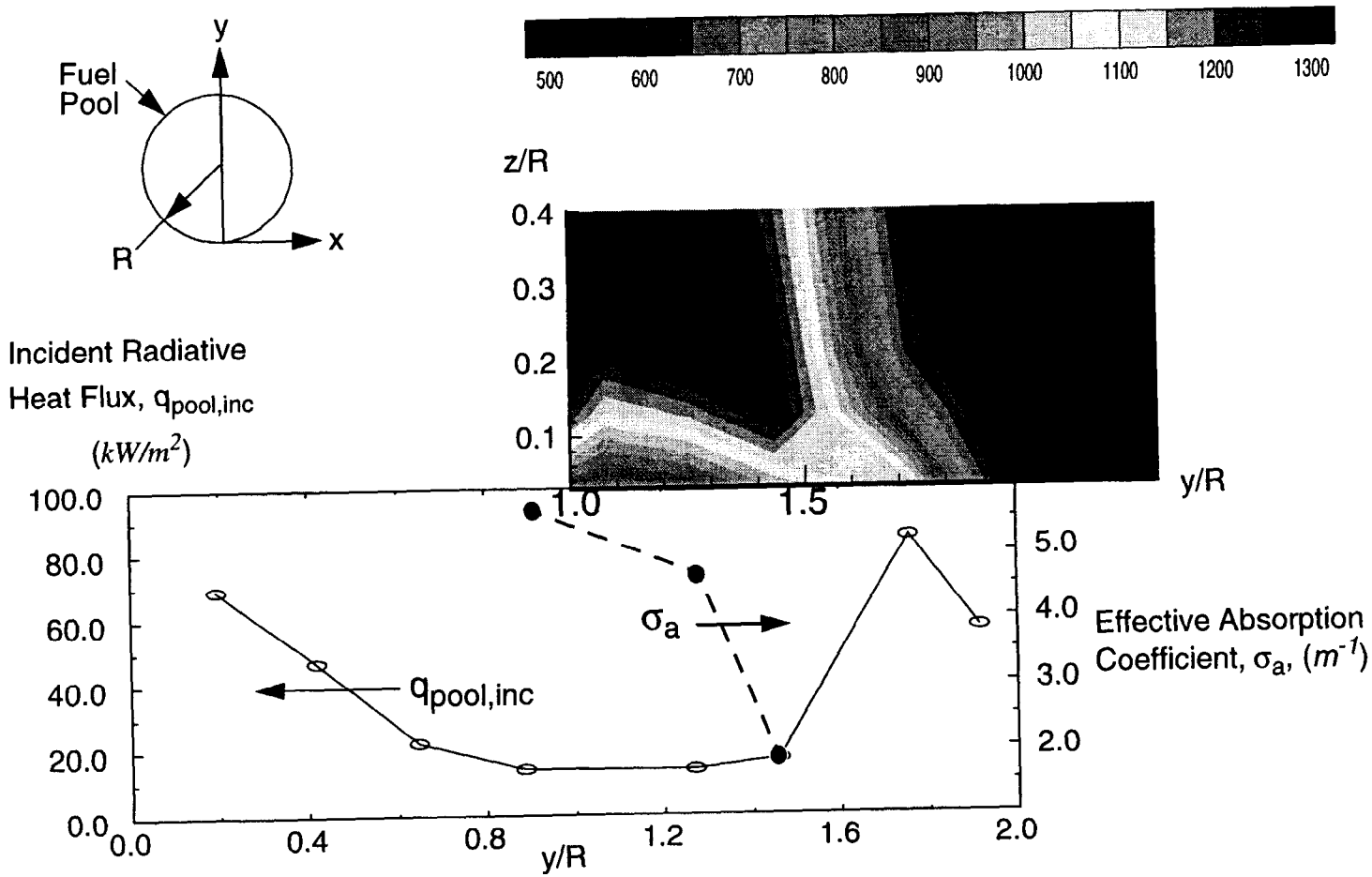

Figure 4.16: Radiative Property Estimates

Property	JP4	JP8
Approximate Chemical Formulation	$C_{8.8}H_{20}$	$C_{11.7}H_{23}$
Density @ 20°C, kg/m^3	760	808
Heat of Combustion (MJ/kg)	43.6	43.2
Boiling Temperature T_{boil} (K)	488	430
Heat of Evaporation (kJ/kg) at average T_{boil}	252	280
Heat Capacity (J/kgK)	2560	2690
Forced Evaporation Rate (kg/m^2s)	0.069	0.060

Table 4.1: Physical Properties of JP4 and JP8 Aviation Fuel

Grid #	ΔX Across Pool (m)	ΔY Across Pool (m)	ΔZ Above Pool (m)	Aspect Ratio = $\frac{\Delta x}{\Delta z} = \frac{\Delta y}{\Delta z}$	Comments
1	1.0	1.0	0.5	2.0	No Gradient Resolution Symmetric Base
2	1.0	1.0	0.2	5.0	Gradient Resolution Small Asymmetries
3	1.0	1.0	0.1	10.0	Gradient Resolution Large Asymmetries
4	0.5	0.5	0.2	2.5	Puffing Fire Symmetric Base
5	0.75	0.75	0.2	3.75	Steady Fire Volume Symmetric Base

Table 4.2: Grids Used in Numerical Simulation of Pool Fires

Coefficient a(i) i=1,5	480	379	49.2	475	1.96
Coefficient b(i) i=1,5	-19.3	28.7	-8.31	-48.3	-59.7
Coefficient c(i) i=1,4	12.7	-30.9	90.8	58.3	-
Coefficient d(i) i=1,4	126	-209	132	-4.62	-
Coefficient e(i) i=1,4	87.4	-5.20	2.19	-140	-

Table 4.3: Coefficient Values for JP8 Temperature Correlation

5.0 Integration of Fire Models into RACTRM

The risk assessment compatible fire models were developed to provide heat flux to a surface in both stand-off and fully-engulfing fire scenarios. Both fire models were integrated into the Risk Assessment Compatible Thermal Response Model (RACTRM)[30]. RACTRM uses the fire models to calculate the heat flux to the surface and then solves the coupled radiation-conduction heat transfer problem. RACTRM was developed to perform computationally efficient risk assessment compatible fire safety analysis of the B52.

5.1 Stand-Off Fire Model

The stand-off fire model has been integrated into the RACTRM code. As discussed in Chapter 3, this model calculates the view factors for both a no-wind condition and a wind condition. In the wind condition, the model calculates the angle of tilt of the fire, the distance downstream which the wind drags the fire, and the height of the fire. The model also calculates three view factor orientations corresponding to positions upwind, downwind, and crosswind. In the case of an arbitrary wind direction, additional logic was included to combine the upwind, downwind, and crosswind view factors based on the wind direction. However, a fire scenario did occur which the model could not treat. This case involved a pool which was situated behind a surface such that the surface could not see the fire directly above the pool, but it did see flames that the wind dragged to locations within the field of view of the surface. For this case, the model returned a view factor of zero because the surface did not face the pool. Since the surface is heated by the portion of the fire that it does see, the model was modified to allow for an arbitrary wind direction.

For an arbitrary wind direction, the fire was broken into a set of overlapping elliptical rings that are overlaid in the direction of the wind. The view factor for the tilted ellipse is calculated by summing the view factors from thin slices of individual elliptical rings. Originally this model calculated view factors for circular cross sections. An equivalent elliptical cross section view factor is found by defining a circle that has the same distance to the edge and the same tangent angles. One circle is oriented along the major and another circle is oriented along the minor axes and the vector sum of the two view factors are combined. Each section of the elliptical rings is combined with the dot product of the surface normal during the summation so that surface to fire orientation, *i.e.* self shading, is accounted for in this approach. Once the view factor has been determined, the heat flux to the surface is found from Equation 3.1.

5.2 Fully-Engulfing Fire Model

The fully-engulfing fire model has also been integrated into the RACTRM code. It was necessary to include logic to determine if the object is fully-engulfed by the fire. In the no-wind case, the object must be positioned within a circle whose radius is equal to the pool radius. In the wind case, the object must be positioned within an ellipse with the major axis equal to the calculated wind-drag diameter and the minor axis equal to the pool diameter.

As discussed in Chapter 4, the fully-engulfing fire model provides the heat flux to a surface by using a distribution of temperatures and a 1-D radiation model. Using the correlations presented in Chapter 4, a temperature distribution is obtained along a normal vector to the surface. For a wind condition, the temperature distribution is obtained by shifting, rotating, and scaling the no-wind temperature distribution based on the stand-off fire model expressions for angle of tilt, wind drag, and height.

There are three sections of subroutines within the fully-engulfing fire model. The first section determines a distribution of points and corresponding temperatures along a normal vector to the object surface. The driver subroutine is called *heatflux* and contains the following arguments:

subroutine heatflux(ro,xin,yin,zin,th1,th2,th3,hf,tmax,ws,thw,dxf,dyf)

where

ro = fuel pool radius (*m*) - input,

xin, yin, zin = coordinates of object surface from pool center (*m*) - input,

th1,th2,th3 = direction angles of normal vector to surface (0-Π radians) - input,

hf = heatflux (W/m^2) - output,

tmax = maximum temperature (*K*) along the normal vector - output,

ws = wind speed (*m/s*) - input,

thw = wind angle (radians) - input,

dxf, dyf = *x* and *y* locations (*m*) of pool center from nosetip of airplane - input.

Given a surface location, a distribution of points along a normal vector is determined. If the wind speed is greater than zero, the input surface location is shifted, rotated, and scaled to the equivalent no-wind position by calling *subroutine wind*. A serious of checks are performed to determine if the normal vector of points crosses either the edge of the fire or the ground. Then the corresponding temperatures inside the fire are determined from the correlations (*subroutine corr*). If the edge of the fire is reached, ambient temperature (300 *K*) is specified. If the ground is reached inside the pool, the fuel pool temperature (480 *K*) is specified, and if the ground is reached outside the pool, the ground temperature is determined from the ground temperature model (*subroutine groundt*). Two other routines (*subroutine viewh* and *subroutine downwind1*) were written to determine the view factor used in the ground temperature model. Finally, the temperature distribution is used by the 1-D radiation model (*subroutine rad2flx*) to determine the heat flux to the surface.

5.3 Assessment of Fully-Engulfing Fire Model Performance

To assess the improvement yielded by the present approach over previous techniques (*i.e.* the method described in Chapter 2), results from both methods are compared with experimental data for three fire scenarios. These scenarios correspond to conditions observed during experiments at NAWC - China Lake. Two of these scenarios are from the

Container Test Series. The remaining scenario is from the Mock Fuselage Test Series. All scenarios use JP8 fuel in a circular pool.

5.3.1 Scenarios 1 and 2

The objects of interest in both of these scenarios is a 1 *m* diameter, 1.5 *m* long weapon container-sized cylinder positioned on its side and located relative to an 18.9 *m* diameter fuel pool as shown in Figure 5.1. The lower edge of the cylinder is 10 *cm* from the fuel. Data include the incident heat flux to both ends (top and bottom) and at three radial locations (90°, 180° and 270°) located at the axial mid-section of cylinder. Wind speed and direction for both scenarios are also shown in Figure 5.1. The two scenarios correspond to winds directed approximately 45° from the axis of the cylinder and winds in the same approximate direction as the axis of the cylinder for scenarios 1 and 2, respectively. Wind data were acquired 5.5 *m* from the ground level and 10 *m* from the edge of the pool along a vector 150° from the reference axis.

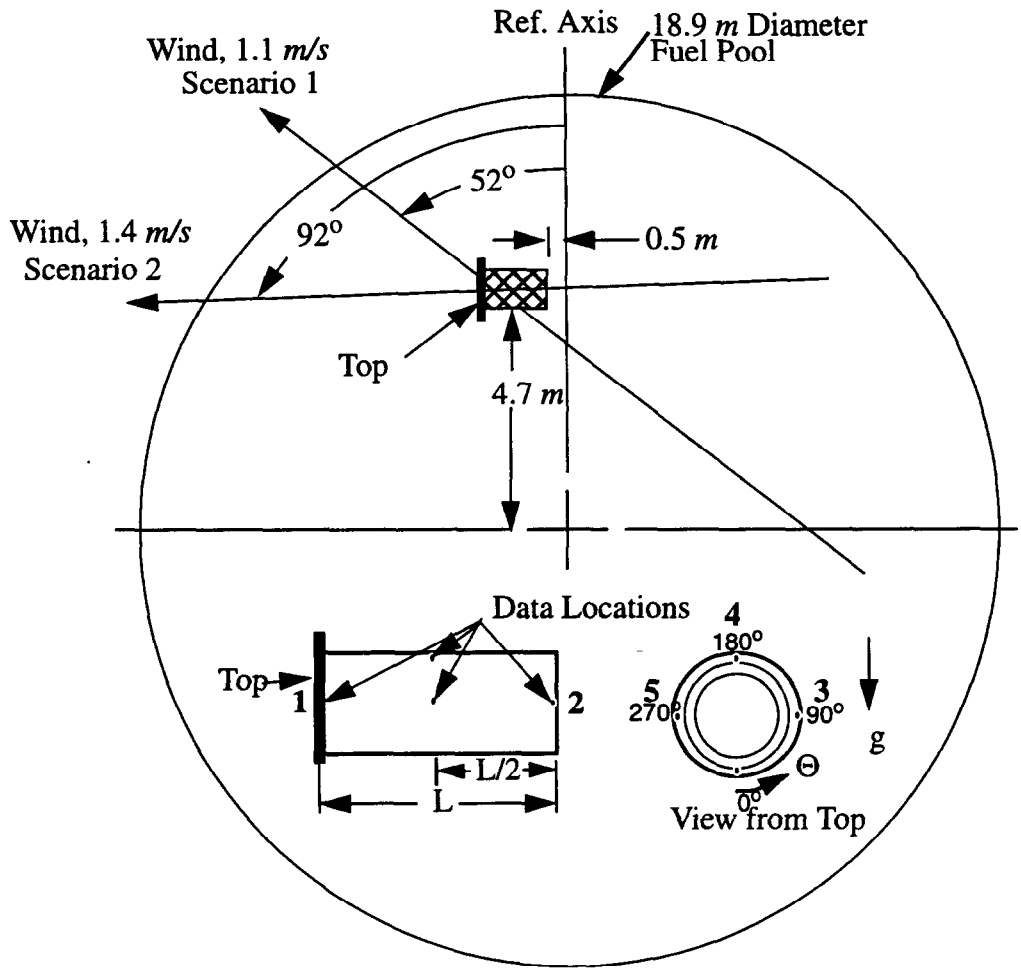

Figure 5.1: Object Position and Orientation for Scenarios 1 and 2

5.3.2 Scenario 3

The third scenario involves a 3.6 *m* diameter, 19 *m* long cylinder (the approximate size of an aircraft fuselage) located on its side and positioned relative to a 9.45 *m* diameter fuel pool as shown in Figure 5.2. The lower edge of the cylinder is 0.3 *m* from the fuel. Data include the incident heat flux to cylinder at radial locations every 45° at the axial mid-section (*i.e.* plane of reference axis) of the cylinder. Average wind speeds of 2.1 *m/s*, in the average direction shown in Figure 5.2, were present during the experiment. Wind data were acquired at elevations of 1.8 *m*, 5.5 *m*, and 9.1 *m* from the ground level at two locations10 *m* from the edge of the pool along vectors -140° and 100° from the reference axis.

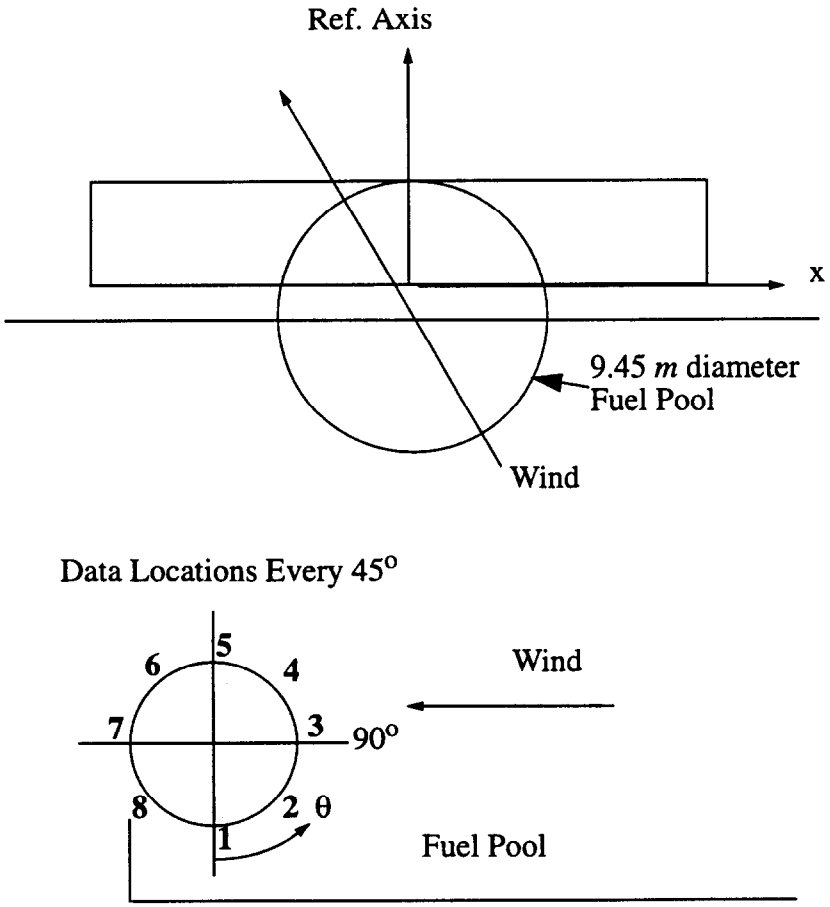

Figure 5.2: Object Position and Orientation for Scenario 3

The incident heat flux to the objects was determined using the RACFMs described in the previous chapter as well as the previous technique which relies on Monte Carlo sampling of the *pdf* presented in Chapter 2. The Monte Carlo technique was performed using random numbers that were generated by the linear congruential method described by Knuth[31]. The *pdf* of the distribution obtained during this procedure agrees very well with the *pdf* presented in Chapter 2, as shown in Figure 5.3. Results were selected at random from the distribution shown in Figure 5.3.

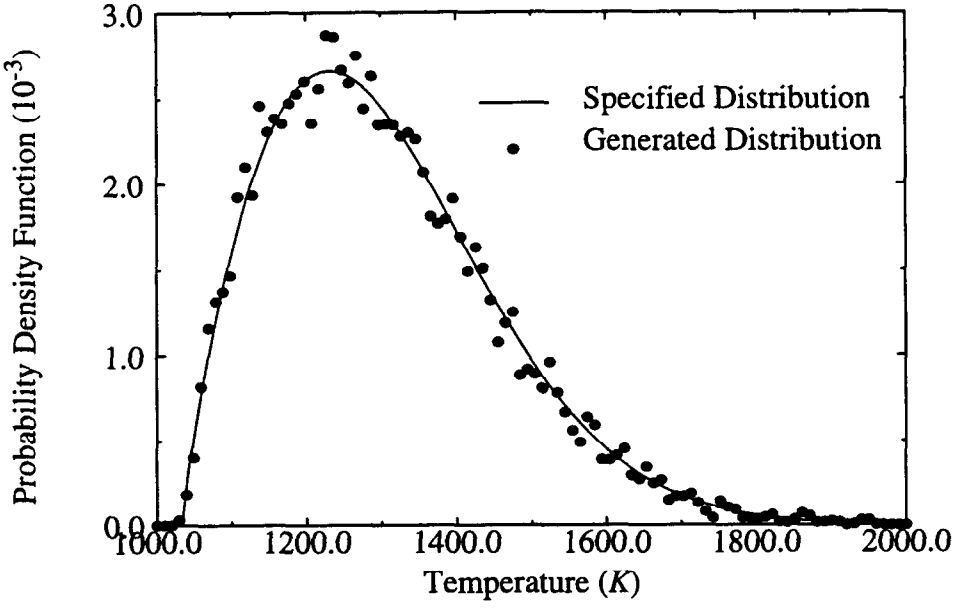

Figure 5.3: Comparison of Specified and Sampled Fire Temperature Distributions

A comparison of the results is shown in Table 5.1. Scenarios 1 and 2 are from the same test series and differ only in the direction and speed of the wind. The measured and predicted values for these two cases were not significantly different and were therefore combined. In every case except for one, the values predicted by the RACFM are closer to the experimental values than those obtained using probabilistic technique. Since the probabilistic method does not include any physics (other than approximate bounds of observed temperatures), the results obtained for a single scenario have no bearing on the actual behavior of the fire under the configuration and environmental conditions of the fire being considered. Large errors can therefore be expected when a single scenario is considered.

Although the RACFMs represent a significant improvement over previous techniques, phenomena not presently included in these models are still sources of discrepancy between the results from the RACFM and the experimental data. The values predicted by the RACFM are comparable, but higher than the experimental values for the container tests.

The largest differences are observed at data locations 2 and 3 which are both located towards the interior of the flame zone. A significant reduction in the radiative flux can be expected in these regions due to the combined presence of a comparatively colder fuel surface and a reduction in flame cover. Since the radiation calculation is only performed along a line-of-sight normal to the object, the influence of the fuel surface is conservatively neglected. Despite this conservatism, the RACFM results agree significantly better with the experimental data than those from the probabilistic technique which over predict the heat flux by greater than a factor of four. Due to the lower temperature limit in the probabilistic distribution, previous techniques will never yield heat flux results below approximately 60 kW/m^2, which is almost a factor of two larger than the measured heat flux at location 3 on the container.

Data Location	Incident Radiative Heat Flux, kW/m^2		
	Exp.	RACFM	Prob.
Scenarios 1 and 2			
1	60	70	128
2	53	112	237
3	34/37	91	140
4	93/96	132	243
5	63/65	92	91
Scenario 3			
1	41	113	162
2	115	134	100
3	233	106	95
4	209	104	80
5	147	102	87
6	91	103	147
7	104	99	162
8	142	121	206

Table 5.1 Comparison of Experimental and Model Results

The differences between the RACFM and the experimental data are more pronounced for scenario 3. In this scenario, the RACFM under predicts the heat flux in locations 3 and 4. Within this region, the flames are impinging on the fuselage resulting in increased convective heat transfer and improved mixing (which in turn increases the temperature and hence the radiative heat flux.) Both of these mechanisms are not presently represented in the model since the flow field is not predicted. Given this simplification, convective coupling, which includes: 1) changes in the geometry of the flame zone due to the presence of an object; and 2) object-induced turbulence which occurs when the presence of an object alters/and often enhances the flow, mixing, and hence combustion processes within the fire; can not be represented by present RACFMs. RACFM estimates in cases where convective coupling are important, such as scenario 3, will therefore include significant uncertainty. Increases in the heat flux approaching a factor of three have been observed due to phenomena resulting from convective coupling.

Presently, the accuracy of the fire model predictions are within 20-30% when significant multidimensional effects or fire-object coupling effects are not present and within a factor of two when these features are important. The addition of a computationally efficient strategy for modeling convective coupling is required to improve the accuracy of the existing models. Such strategies are thought to be possible and are presently under development.

6.0 Future Work

The development of the Stand-Off Model and the Fully-Engulfing Fire Model has improved the Risk Assessment Compatible Fire Models beyond past models. For the fully-engulfing fire scenario, the model was upgraded from a single effective fire temperature and heat flux determined from black body radiation to a temperature distribution based on correlations and heat flux determined from a 1-D radiation model. Future plans include developing a 2-D fire field model to determine the temperature distribution. A fire field model would allow two important effects to be included: the influence of an object on a fire flow field; and the influence of off-axis component of wind which test series have shown to be a dominant feature. The heat flux calculation could also be improved by extending the 1-D radiation model to a 2-D radiation model. For the stand-off fire scenario, the current model could be improved by using experimental data to assess the validity of the approach and the assumption of azimuthal symmetry. The flame emissive power could be evaluated using the combination of stand-off flux measurements and infrared (IR) video. The assumed flame shape could also be improved by using time averaged photos as well as IR and standard videos.

References

[1]Clarke, R. W., et al., "Severities of Transportation Accidents," SLA-74-0001, Sandia National Laboratories Report, July 1976.

[2]Holen, J., Brostrom, M., and Magnussen, B. F., "Finite Difference Calculation of Pool Fires," 23rd Int. Symp. Comb., The Combustion Institute, pp. 1677-1783, 1990.

[3]Launder, B. E. and Spalding, D. B., *Computer Methods in Applied Mechanics and Engineering*, 3, p. 269, 1974.

[4]Magnussen, B. F., Hjertager, B. H., Olsen, J. G., and Bhaduri, D., "The Eddy Dissipation Concept," 17th Int. Symp. Comb., The Combustion Institute, pp. 1383-1398, 1979.

[5]Magnussen, B. F., "Particulate Carbon Formation During Combustion," Plenum Publishing Corporation, 1981.

[6]Shah, N. G., "The Computation of Radiation Heat Transfer," Ph.D. Thesis, University of London, Faculty of Engineering, 1979.

[7]Gritzo, L.A., Nicolette, V.F, Moya, J.L., Skocypec, R.D., and Murray, D. "Wind-Induced Interaction of a Large Cylindrical Calorimeter and an Engulfing JP-8 Pool Fire," Proceedings of the Symposium on Thermal Sciences in Honor of Chancellor Chang-Lin Tien, Berkeley, CA, November 14, 1995.

[8]Gritzo, L.A., Nicolette, V.F., Tieszen, S.R., and Moya, J.L. "Heat Transfer to the Fuel Surface in Large Pool Fires," Transport Phenomenon in Combustion, S.H. Chan, ed., Taylor and Francis, 1995.

[9]Gritzo, L.A., and Nicolette, V.F. "Coupled Thermal Response of Objects and Participating Media in Fires and Large Combustion Systems," Numerical Heat Transfer, Part A, 28:531-545, 1995.

[10]Mudan, K. S. and Croce, P. A., "Fire Hazard Calculations for Large Open Hydrocarbon Fires," *SFPE Handbook of Fire Protection Engineering*, Chapter 4, Section 2, 1988.

[11]Raj, P. P. K. and Kalelkar, A. S., "Assessment Models in Support of the Hazard Assessment Handbook," Arthur D. Little, Inc. AD-776-617, January 1974.

[12]Hagglund, B. and Persson, L., "The Heat Radiation from Petroleum Fire," FOA Rapprt: Forvarets Forskningsansstalt, Stockholm, 1976.

[13] Gritzo, L. A. and Tieszen, S. R., "Turbulent Structures in Large Pool Fires," Invited Presentation at the 32nd Meeting of the Society of Engineering Sciences, New Orleans, LA, October 30-31, 1995.

[14]Thomas, P. H.,"The Size of Flames from Natural Fires," 9th International Combustion Symposium, Combustion Institute, Pittsburgh, PA, pp. 844-859, 1963.

[15]American Gas Association, "LNG Safety Research Program," Report IS 3-1, 1974.

[16]Mudan, K. S., "Geometric View Factors for Thermal Radiation Hazard Assessment," *Fire Safety Journal*, Vol. 12, pp. 89-96, 1987.

[17]Sherman, M. P., "Radiant heat transfer from Large Hydrocarbon Pool Fires - State-of-the-art," Internal Memo to J. L. Moya, March 8, 1995.

[18]Sherman, M. P., "Heat transfer from large hydrocarbon pool fires - State-of-the-art II," Internal Memo to J. L. Moya, April, 18, 1985.

[19]Sherman, M. P., "Temperature Curve Fit in the Flame for Large JP-4 Pool Fire," Internal Memo to J. L. Moya, May 4, 1995.

[20]Gritzo, L.A., Gill, W., and Keltner, N., "Thermal Measurements to Characterize Large Fires," Proceedings of the 41st International Instrumentation Symposium, May 7-11, 1995, Denver, Co.

[21]Nicolette, V. F., "Fire Modeling Investigation of JP4/JP8 Differences," Internal Memo to J. L. Moya, May 6, 1995.

[22]Jandel Scientific Company, "TableCurve 2D," Version 2.0, San Rafael, CA, 1994.

[23]Sherman, M. P., "The ground temperature around a pool fire," Internal Memorandum to J. L. Moya, August 25, 1995.

[24]Nakos, J. T. and Keltner, N. R., "The Radiative Partitioning of Heat Transfer to Structures in Large Pool Fires," HTD-Vol. 106, Heat Transfer Phenomena in Radiation, Combustion and Fires, R.K. Shah, ed., ASME, 1989.

[25]Siegel, R. and Howell, J., Thermal Radiation Heat Transfer, 2nd ed., Hemisphere Publishing Co., p 513., 1981.

[26]Schuster, A., "Radiation Through a Foggy Atmosphere," *Astrophysics Journal*, Vol. 21, pp. 1-22, 1905.

[27]Eddington, A. S., "The Internal Constitution of the Stars," Dover, New York, 1959.

[28]Longenbaugh, R. S. and Matthews, L. K., "Experimental and Theoretical Analysis of the Radiative Transfer within a Sooty Pool Fire," SAND86-0083, Sandia National Laboratories, Albuquerque, NM, 1986.

[29]Felske, J. D. and Tien, C. L., "Calculation of the Emissivity of Luminous Flames," Combustion Science and Technology, Vol. 7, pp. 25-31, 1973.

[30]Suo-Anttila, A. J., "Risk Assessment Compatible Thermal Response Model," Sandia National Laboratories Report, To be Published 1997.

[31]Knuth, D. E., *Art of Computer Programming: Semi-Numerical Algorithms*, Addison-Wesley, 1982.

[32]Rein, R. G, Sliepcevich, C. M., and Welker, J. R., "Radiation view factors for tilted cylinders," *Journal of Fire Flammability*, Volume 1, pp. 140-153, 1970.

Appendix A - Radiation View Factors from a Plane Element to a Tilted Cylinder

The shape of the radiating plume of a pool fire under wind conditions is approximated by a tilted cylinder as shown in Figure 3.1. Analytical expressions of the radiation view factors from a plane element to a tilted cylinder were first obtained by Mudan.[16] Mudan provided view factors in the plane of tilt (downwind and upwind directions) and in the plane perpendicular to the tilt direction (crosswind direction) to a vertical plane element and a horizontal plane element.

Consider a cylinder of radius R, slant height H_w, and tilt angle θ. θ is defined positive in the downwind direction and negative in the upwind direction. As discussed in Chapter 3, the radius of the cylinder varies since the cross section of the cylinder along the ground is modeled as an ellipse. The minor axis diameter D is perpendicular to the plane of tilt and the major axis diameter D_{max} is in the plane of tilt. Given a plane element a distance X from the center of the cylinder, view factors from the element to the tilted cylinder are shown below.

In both the upwind and the downwind cases, horizontal and vertical view factors are defined as follows:

$$\pi F_v = \left(\frac{a\cos\theta}{b - a\sin\theta}\right)\left(\frac{a^2 + (b+1)^2 - 2b(1 + a\sin\theta)}{\sqrt{AB}}\right)\left(\text{atan}\left\{\sqrt{\frac{A}{B}}\sqrt{\frac{b-1}{b+1}}\right\}\right)$$
$$+\left(\frac{\cos\theta}{\sqrt{C}}\right)\left(\text{atan}\left\{\frac{ab - (b^2-1)\sin\theta}{\sqrt{b^2-1}\sqrt{C}}\right\} + \text{atan}\left\{\frac{(b^2-1)\sin\theta}{\sqrt{b^2-1}\sqrt{C}}\right\}\right)$$
$$-\left(\frac{a\cos\theta}{(b - a\sin\theta)}\right)\left(\text{atan}\left\{\sqrt{\frac{b-1}{b+1}}\right\}\right)$$

$$\pi F_h = \text{atan}\left\{\sqrt{\frac{b+1}{b-1}}\right\} - \left(\frac{a^2 + (b+1)^2 - 2(b + 1 + ab\sin\theta)}{\sqrt{AB}}\right)\left(\text{atan}\left\{\sqrt{\frac{A}{B}}\sqrt{\frac{b-1}{b+1}}\right\}\right)$$
$$+\left(\frac{\sin\theta}{\sqrt{C}}\right)\left(\text{atan}\left\{\frac{ab - (b^2-1)\sin\theta}{\sqrt{b^2-1}\sqrt{C}}\right\} + \text{atan}\left\{\frac{\sqrt{b^2-1}\sin\theta}{\sqrt{C}}\right\}\right)$$

where

$$a = \frac{H_w}{R}, \qquad b = \frac{X}{R}$$

$$A = a^2 + (b+1)^2 - 2a(b+1)\sin\theta$$

$$B = a^2 + (b-1)^2 - 2a(b-1)\sin\theta$$

$$C = 1 + (b^2 - 1)(\cos\theta)^2 \ .$$

In the limit as $\theta \to 0$, the above equations for a tilted cylinder reduce to those for a vertical cylinder which appear in several textbooks. Setting $\cos\theta = 1$ and $\sin\theta = 0$, the following equations result.

$$\pi F_v = \left(\frac{a}{b}\right)\left(\frac{a^2+b^2+1}{\sqrt{AB}}\right)\left(\text{atan}\left\{\sqrt{\frac{A}{B}}\sqrt{\frac{b-1}{b+1}}\right\}\right) + \frac{1}{b}\text{atan}\left\{\frac{a}{\sqrt{b^2-1}}\right\} - \frac{a}{b}\text{atan}\left\{\sqrt{\frac{b-1}{b+1}}\right\}$$

$$\pi F_h = \text{atan}\left\{\sqrt{\frac{b+1}{b-1}}\right\} - \left(\frac{a^2+b^2-1}{\sqrt{AB}}\right)\left(\text{atan}\left\{\sqrt{\frac{A}{B}}\sqrt{\frac{b-1}{b+1}}\right\}\right)$$

where

$$A = a^2 + (b+1)^2 \ , \qquad B = a^2 + (b-1)^2 \ .$$

In the cross wind case, horizontal and vertical view factors are defined as follows:

$$2\pi F_v = -\left(\frac{a^2\sin\theta\cos\theta}{2(a^2\sin\theta^2 + b^2)}\right)\left(\ln\left\{\frac{a^2+b^2-1-\frac{2aP}{b}\sin\theta}{a^2+b^2-1+\frac{2aP}{b}\sin\theta}\right\}\right) + \frac{\cos\theta}{Q}\left(\text{atan}\left\{\frac{\frac{ab}{P}+\sin\theta}{Q}\right\}\right.$$

$$\left. + \text{atan}\left\{\frac{\frac{ab}{P}-\sin\theta}{Q}\right\}\right) - \left(\frac{2ab\cos\theta}{T}\right)\left(\frac{S}{\sqrt{S^2-4T}}\right)\left(\text{atan}\sqrt{\frac{b-1}{b+1}}\right)$$

$$+ \left(\frac{ab\cos\theta}{T}\right)\left(\frac{S}{\sqrt{S^2-4T}}\right)\left(\text{atan}\left\{\frac{(a^2+(b+1)^2)\sqrt{\frac{b-1}{b+1}}-(2a)\sin\theta}{\sqrt{S^2-4T}}\right\}\right.$$

$$\left. + \text{atan}\left\{\frac{(a^2+(b+1)^2)\sqrt{\frac{b-1}{b+1}}+(2a)\sin\theta}{\sqrt{S^2-4T}}\right\}\right)$$

$$2\pi F_h = 2\,\mathrm{atan}\left\{\sqrt{\frac{b+1}{b-1}}\right\} + \frac{P\sin\theta}{Q}\left(\mathrm{atan}\left\{\frac{\frac{ab}{P}+\sin\theta}{Q}\right\} - \mathrm{atan}\left\{\frac{\frac{ab}{P}-\sin\theta}{Q}\right\} - 2\,\mathrm{atan}\left\{\frac{\sin\theta}{Q}\right\}\right)$$

$$-\left(\frac{a^2+b^2-1}{\sqrt{S^2-4T}}\right)\left(\mathrm{atan}\left\{\frac{(a^2+(b+1)^2)\sqrt{\frac{b-1}{b+1}}-(2a)\sin\theta}{\sqrt{S^2-4T}}\right\}\right.$$

$$\left. + \mathrm{atan}\left\{\frac{(a^2+(b+1)^2)\sqrt{\frac{b-1}{b+1}}+(2a)\sin\theta}{\sqrt{S^2-4T}}\right\}\right)$$

where

$$P = \sqrt{b^2-1}\,, \quad Q = \sqrt{b^2-(\sin\theta)^2}$$

$$S = a^2+b^2+1\,, \quad T = b^2+a^2(\sin\theta)^2\,.$$

Finally, Rein, Sliepcevich, and Welker,[32] performed numerical integration of view factors to tilted cylinders. In their work, the cross section normal to the axis of the cylinder is circular and the cross section along the ground is elliptical. Therefore, on the ground the minor axis diameter is unchanged by the tilt, but the major axis diameter is increased by a factor of $1/(\cos\theta)$, where θ is the angle of tilt from the vertical. This geometry is a closer approximation to the expected pool fire shape than that of Mudan. Mudan assumes a pool fire geometry with a circular cross section along the ground and along the top of the cylinder. However, since the results of Rein, et al. are in numerical form, it is difficult to determine accurate expressions from logarithmic plots. In addition, their numerical results only included view factors for a vertical target orientation.

Distribution

Copies	Mail Stop	Org.	Name
1	0841	9100	P. J. Hommert
1	0828	9101	T. C. Bickel
1	0841	9102	C. Hartwig
1	0828	9104	R. K. Thomas
1	0865	9105	J. L. Moya
1	0827	9111	W. Hermina
1	0827	9111	C. E. Hickox
1	0834	9112	A. C. Ratzel
1	0835	9113	S. N. Kemkpa
1	0826	9114	R. O. Griffith
1	0825	9115	W. H. Rutledge
5	0825	9115	A. R. Lopez
1	0836	9116	C. W. Peterson
5	0836	9116	L. A. Gritzo
1	0836	9116	S. R. Tieszen
1	0836	9116	V. F. Nicolette
2	1146	6442	M. P. Sherman
1	0834	9112	T. Y. Chu
1	0555	9135	W. Gill
1	0405	12304	D. D. Carlson
1	0717	6342	J. A. Koski
1	0748	6413	S. P. Nowlen
1	0483	2165	R. E. Glass
1	0447	2111	A.L. Hillhouse
1	9018	8940-2	Central Technical Files
2	0899	4916	Technical Library
2	0619	12690	Review and Approval desk For DOE/OSTI

1 Director, Defense Special Weapon Agency
Attn: Lt. Col. Gil Rodriguez
6801 Telegraph Road
Alexandria, VA 22310-3398

1 Director, Defense Special Weapon Agency
Attn: James V. Brackett
6801 Telegraph Road
Alexandria, VA 22310-3398

1 Director, Defense Special Weapon Agency
Attn: Major John A. Dorian
6801 Telegraph Road
Alexandria, VA 22310-3398

1 U.S. Coast Guard R&D Center
Attn: L. Nash
1082 Shennecossett Road
Groton, CT 06340-6096

1 U. S. Department of Energy
Albuquerque Operations Office
Albuquerque Headquarters
Attn: H. T. Season
P. O. Box 5400
Albuquerque, NM 87115

1 U. S. Department of Energy
Albuquerque Operations Office
Albuquerque Headquarters
Attn: R. O. Gergen
P. O. Box 5400
Albuquerque, NM 87115

1 U. S. Department of Energy
Albuquerque Operations Office
Albuquerque Headquarters
Attn: Roger Cartee
P. O. Box 5400
Albuquerque, NM 87115

1 U. S. Department of Energy
Albuquerque Operations Office
Albuquerque Headquarters
Attn: Karl Rueb
P. O. Box 5400
Albuquerque, NM 87115

1 Exxon Production Research
Attn: J. Barnhart
3319 Marcer St.
Houston, TX 77027

1 JM Technical
Attn: J. Mansfield
531 NW Canyon Drive
Redmond, OR 97756

1 K-Tech Corp.
Attn: Ned Keltner
901 Pennsylvania NE
Albuquerque, NM 87110

1 Lawrence Livermore National Laboratories
Attn: Doug Stevens
P. O. Box 808, L-85
Livermore, CA 94550

1 Logicon RDA
Attn: Art Barondes
6940 South Kings Highway, Suite 210
Alexandria, VA 22310

1 Los Alamos National Laboratories
Attn: Ron Flurry
P. O. Box 1663, MSC931
Los Alamos, NM 87545

1 Los Alamos Technical Associates
Attn: Lou Reidl
2400 Louisiana Blvd. NE
Building 1, Suite 400
Albuquerque, NM 87110

1 Commander
Naval Air Warfare Center
Attn: Doug Murray
Code 528200D
China Lake, CA 93555

1 Commander
Naval Air Warfare Center - Weapons Division
Attn: Leo Budd
Code 418300D
China Lake, CA 93555-6001

1 Commander
Naval Air Warfare Center - Aircraft Division
Attn: Bill Leach
Code 43520, B562-3
Lakehurst, NJ 08733-5100

1 Commander
Naval Surface Warfare Center - Carderock Division
Attn: Usman Sorathia
Code 643, Bldg. 60
9500 MacArthur Blvd.
Bethesda, MD 20084-5000

1 NWI
Attn: Col. John Curry, Technical Director
1651 First Street SE
Kirtland AFB, NM 87117

1 NWI
Attn: Dr. Dermod Kelleher, Technical Director
1651 First Street SE
Kirtland AFB, NM 87117

1 NWIE
Attn: Michael Martinez
1651 First Street SE
Kirtland AFB, NM 87117

1 PLG Inc.
Attn: David Johnson
4590 MacArthur Blvd. Suite 400
Newport Beach, CA 92660

1 Wright Laboratories
Attn: M. Bennett
FIVS Bldg. 63
1901 Tenth Street
Wright Patterson Air Force Base, Ohio 45433-7605